ACS NANO

www.acsnano.org

ARTICLE

Remodeling the Tumor Microenvironment: An Emerging Paradigm for Reinvigorating Immunologically Cold Tumors and Advancing Cancer Immunotherapy

Jia Zeng,[§] Xinning Fang,[§] Yuhan Li, Qi Yan, Yitong Li, Han Yu, Xiangyu Zhao, Mengyuan Xu, Zhenghong Wu,* and Xiaole Qi*

Cite This: *ACS Nano* 2026, 20, 636−656

Read Online

ACCESS | Metrics & More | Article Recommendations | Supporting Information

ABSTRACT: The treatment of solid tumors often faces significant hurdles. These include inefficient drug delivery due to a lack of specific targets and difficulties in penetrating tumors, as well as inadequate immune activation exacerbated by immunosuppressive tumor microenvironments. This study introduces a biomimetic system that employs a fusion membrane (FM) composed of hyaluronidase-decorated bacterial-derived outer membrane vesicles (OMVs) and PD-L1 knockout cancer-derived cell membranes (CCMs). By leveraging the affinity of the OMVs for neutrophils, the FMs can efficiently navigate to tumor sites. The hyaluronidase decoration further overcomes the fibrotic matrix barrier, facilitating the infiltration of immune cells and therapeutic agents. Meanwhile, the genetically edited CCMs not only ensure precise homologous tumor targeting but also minimize the introduction of exogenous immunosuppressive factors. Each component of the FM provides an abundance of antigens, amplifying immune enhancement and addressing the issue of inadequate immune responses. In multiple tumor models, our results demonstrated that FM system exhibited superior tumor targeting, penetration, and immune activation. When combined with chemotherapy and immunotherapy, it led to significant tumor volume reduction and survival benefits. This advanced biomimetic platform integrates precise targeting, efficient drug delivery, and potent immune stimulation, offering a promising approach for solid tumor treatment.

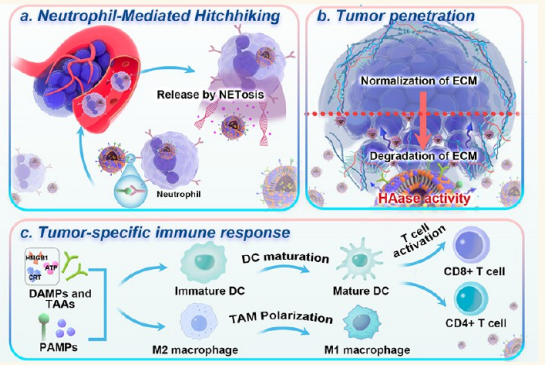

KEYWORDS: *malignant solid tumors, biomimetic nanodelivery system, neutrophil hitchhiking, extracellular matrix destruction, immune activation*

1. INTRODUCTION

Malignant solid tumors continue to pose a formidable challenge, and the pursuit for precise and efficient delivery of antitumor agents remains a focal point of research endeavors. While enhanced permeability and retention (EPR) effect-based nanoparticles have advanced tumor targeting, their clinical translation is hindered by passive accumulation and uneven intratumoral distribution.[1] The active transport and retention (ATR) principle has emerged as a biology-driven alternative,[2] utilizing transcytosis, vesicle-vacuolar organelles, migrating cell effects, and immune cell inflammatory tropism to enhance the targeting efficiency.[3−6] However, even when substantial payloads reach the tumor, their spread is often arrested by a dense, fibrotic stroma.[7] Rapidly proliferating tumor cells drive excessive connective tissue hyperplasia, forming an hyaluronic acid (HA)-rich extracellular matrix (ECM),[8−11] which physically blocks immune infiltration and drug penetration, making ECM disruption essential for therapeutic efficacy.[12] Clinically, chemo-immunotherapy has largely replaced monotherapy due to its ability to enhance antigenicity and reduce chemoresistance[13] but not all cancers response optimally. "Cold tumors", characterized by low antigen presentation, poor immune infiltration, and an immunosuppressive microenviron-

Received: August 27, 2025
Revised: December 8, 2025
Accepted: December 9, 2025
Published: December 18, 2025

https://doi.org/10.1021/acsnano.5c14644
ACS Nano 2026, 20, 636−656

Scheme 1. Schematic Illustration of the Randomizable Paradigm "Slot Machine" for Tumor Therapy Based on the FM System, Encompassing Distribution Regulation, Immunotherapy, Delivery Application, and Diseases Diversity

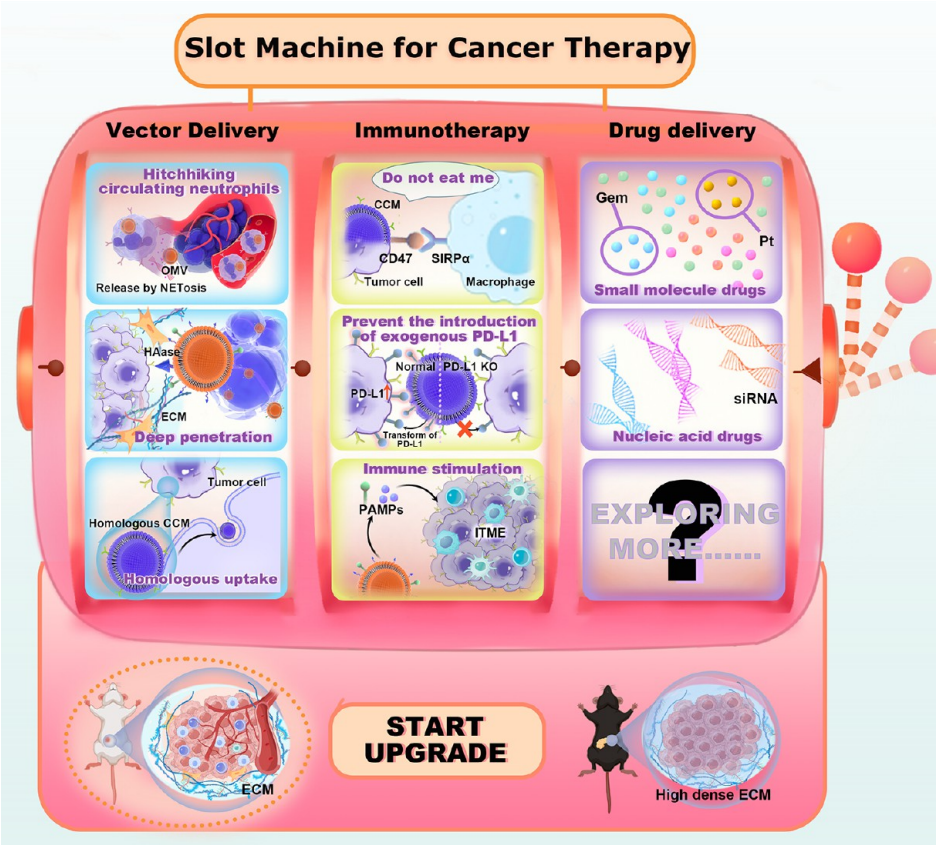

ment,[14] remain resistant to immunotherapy and are linked to worse outcomes. These refractory tumors highlight the need for advanced nanodelivery systems that simultaneously achieve effective intratumoral distribution and robust immune activation to realize meaningful antitumor effects.

Recently, biomimetic nanovesicles (BNVs) have emerged as a highly promising nanodelivery platform, showcasing considerable potential across various applications. Produced by cells across all kingdoms of life, BNVs derived from mammalian cells and bacteria have drawn particular attention for pharmaceutical development.[15] These natural vesicles inherit biological information from their progenitors, enabling crucial roles in intercellular communication and functional molecular transport.[16,17] Unlike artificial liposomes, BNVs excel in biocompatibility and functional adaptability. For instance, surfaces functionalized with hydrophilic PEG or phagocytosis-inhibiting peptide successfully enable immune escape and extent the half-life of BNVs.[18] Cell membrane camouflage strategies further minimize phagocytosis while enhancing targeting specificity.[19] By conjugating ligands, BNVs achieve antigen shielding,[20] specific antigen capturing,[21] and inflammatory site hitchhiking.[22] BNVs exhibit infinite possibilities for customization via various modification techniques, and their unique properties make them a highly attractive option for advanced nanodelivery systems, poised to revolutionize therapeutic strategies.

Consequently, we endeavor to establish an innovative biomimetic nanodelivery system to overcome the hurdles in solid tumor drug development. This system leverages BNVs with distinct properties and functions as modular building blocks, collectively constructing a versatile and customizable carrier platform. As the cornerstone of this system, we selected bacterial-derived outer membrane vesicles (OMVs) and specific cancer-derived cell membranes (CCMs), integrating them through advanced hybrid membrane fusion techniques. OMVs naturally exploit neutrophil (NE) hitchhiking via TLR4 recognition—an exemplary ATR strategy,[23] and activate innate immune pathways, serving as direct immunotherapeutic adjuvants.[24−26] However, standalone OMVs suffer from nonspecific uptake,[27] limiting their targeting precision. CCMs, devoid of genetic information, are emerging as another tumor vaccine candidate due to their homologous targeting and abundant tumor antigens supply.[28] Their tumor-associated surface antigens endow them with immune escape abilities,[29] yet inadvertently induce immunosuppression. Therefore, the membrane fusion strategy synergizes the strengths of both parent materials while circumventing their individual drawbacks,[30] achieving superior intratumoral delivery and immune activation.

Our fusion membrane (FM) system is further tailored through genetic engineering to incorporate specific proteins, fulfilling customized objectives with precision, including deep tumor penetration and immunosuppression reversal. Specifically, hyaluronidase (HAase) is decorated on the surface of the OMVs (HAase-OMV) to disrupt the protective ECM barrier, facilitating the infiltration of immune cells and therapeutic agents. Meanwhile PD-L1 is knockout from CCMs (CCM^{KO}) to prevent any unintended immune surveillance that might arise from exogenous PD-L1 introduction.[31] This "subtraction-addition" dual editing-genetic deletion plus functional grafting

https://doi.org/10.1021/acsnano.5c14644
ACS Nano 2026, 20, 636−656

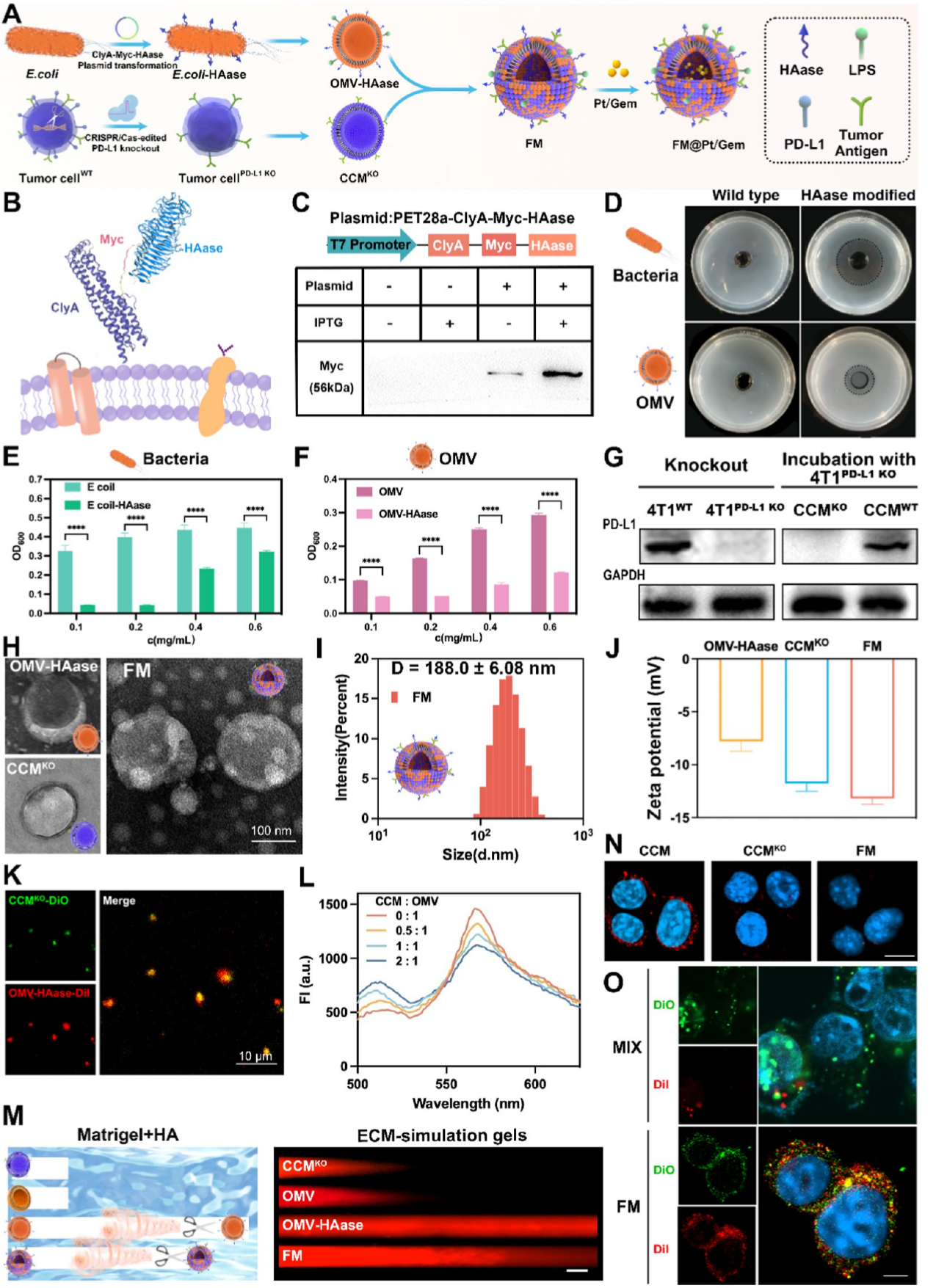

Figure 1. Construction and characterization of tailored and modified FM. (A) Schematic illustration of the FM from OMV-HAase and CCM^{KO} and its loading capacity. (B) The conformational arrangement of ClyA-HAase on the bacterial surface was simulated using ChimeraX software. (C) Detection of expressed Myc tag of ClyA-Myc-HAase on the OMV by Western blot. (D) Qualitative analysis for

https://doi.org/10.1021/acsnano.5c14644
ACS Nano 2026, 20, 636−656

Figure 1. continued

HAase activity using the HA agarose plate assay. Quantitative estimation of HA scavenging ability using HA degradation spectrophotometric assay for (E) engineered bacteria and (F) OMV-HAase under increasing HA concentration. (G) PD-L1 knockout efficiency and relocation of internalized exogeneous PD-L1. (H) Representative TEM images of OMV-HAase, CCM^{KO}, and FM. (I) Particle size of FM. (J) Zeta-potential comparison of OMV-HAase, CCM^{KO}, and FM. (K) Representative CLSM image of colocalization situation in FM (Green: DiO-labeled CCM^{KO}; Red: DiI-labeled OMV-HAase). (L) Verification of membrane fusion by FRET. (M) Schematic illustration and verification of the penetration capacity of FM within ECM-simulated gel comprising HA and Matrigel (scale bar: 100 μm). (N) PD-L1 expression levels on the $4T1^{KO}$ cell membrane after incubation with CCM, CCM^{KO}, and FM (scale bar: 10 μm). (O) Intracellular colocalization of FM (scale bar: 10 μm).

elevates the FM from simple functional superposition to true functional complementation. As conceptualized in Scheme 1, this platform establishes a randomized "slot machine" paradigm for tumor therapy, operating as a universal "motherboard" with modular customization capabilities. The system progresses through three stages: (1) during in vivo distribution regulation, FM leverages NE-mediated hitchhiking, ECM disruption, and homologous targeting to achieve highly efficient intratumoral accumulation; (2) in the immunotherapy optimization, FM achieves immune evasion, reduction of immunosuppression, and synergistically amplifies immune activation through multimechanistic stimulation; (3) in clinical application, FM accommodates diverse payloads, including small-molecule chemotherapeutics and nucleic acid drugs, enabling personalized combination therapies. Studies across solid tumor models confirm FMs' superiority over a single-membrane system. By unifying delivery precision, stromal barrier disruption, and immune reactivation, this innovation addresses the critical unmet needs of cold tumors and refractory malignancies, positioning FM as a next-generation therapy platform.

2. RESULTS

2.1. Construction and Characterization of FM. A modular nanoplatform was engineered by merging membranes of distinct origins into a single functionalized vesicle, as depicted in Figure 1A. HAase was covalently displayed onto the OMV surfaces via the membrane anchoring protein cytolysin A (ClyA). The conformational arrangement of ClyA-HAase on the bacterial surface was simulated by using ChimeraX software (Figure 1B). Specifically, we engineered a T7 promoter plasmid encoding HAase-ClyA with an intervening flexible Myc-tagged linker (Figure S1). Preliminary verification confirmed HAase expression through Myc tag detection, with Western blot showing a distinct 56 kDa band exclusively in induced samples (Figure 1C). HAase activity was first validated on HA agarose plates. Clear halos indicated robust substrate degradation by engineered *Escherichia. coli* and derived OMVs, whereas wild-type OMVs remained inactive (Figure 1D). Quantitative assay revealed over 85% HA scavenging efficiency by engineered bacteria at low HA concentrations, though activity declined in HA-rich environments due to the growth inhibition caused by osmotic stress and nutrient limitation (Figure 1E). In contrast, the OMV-HAase maintained 50% clearance rates regardless of HA concentration, underscoring the superior environmental robustness of vesicles over living cells (Figure 1F). Next, to preclude PD-L1-mediated immunosuppression, we employed the gene editing technology to knock out PD-L1 on tumor cell membranes. A cas9/sgRNA ribonucleoprotein complex (RNP) was constructed, as shown in Figure S2, and was then delivered into 4T1 cells by transfection. The complete loss of PD-L1 was verified by Western blot (Figure 1G). To broaden the application scope of FM, we further constructed $Pan02^{PD\text{-}L1\ KO}$ cells (Figure S3). When PD-L1-knockout CCM (CCM^{KO}) were incubated with $4T1^{PD\text{-}L1\ KO}$ cells, no expression of PD-L1 was observed, whereas normal CCM (CCM^{WT}) restored membrane PD-L1 expression (Figure 1G). Thus, CCM^{KO} provided a PD-L1-free building block for subsequent assembly.

OMV-HAase and CCM^{KO} were fused by serial coextrusion. Ultrasonication at 40 W, 4 °C, and 20 times extrusion in pH 7.4 PBS yielded optimal vesicle size and fusion efficiency (Figure S4). TEM images revealed intact bilayer vesicles of FM, indicating good compatibility between OMV-HAase and CCM^{KO} (Figure 1H). The particle sizes of OMV-HAase and CCM^{KO} and FM were 186.0 nm, 212.2 nm, and 188.0 nm, respectively, with good uniformity (Figures S5 and 1I). Zeta potentials were separately −7.77 mV, −11.8 mV, and −13.2 mV (Figure 1J). SDS-PAGE verified that FM inherited the majority of the parental membrane proteins (Figure S6). Besides, in representative CLSM images, DiO-labeled CCM and DiI-labeled OMV exhibited pronounced colocalization within FM, providing direct evidence of successful membrane fusion (Figure 1K). To corroborate this observation, we employed fluorescence resonance energy transfer (FRET). OMVs were prelabeled with a donor−acceptor dye pair, and fusion with CCM progressively disrupted the nanometer-scale proximity required for FRET. Consequently, emission at 565 nm decreased markedly, with a more pronounced decline observed as the proportion of CCM increased (Figure 1L). This FRET signal attenuation unequivocally confirms the integration of the two membrane systems during FM formation. Subsequently, the functional integrity postfusion was detected. FM significantly degraded HA and penetrated deeply into the HA matrix, demonstrating a deeper distribution within the gel (Figure 1M). Relative HAase enzyme activities were 110.6 U/mg for the OMV-HAase and 57.1 U/mg for FM, via constructing a relative activity standard curve using commercial hyaluronidase (Figure S7). These two preserved over 65% activity for 36 h under physiological or tumor-mimicking conditions, while free commercial was rapidly inactivated by its protein crown shield (Figure S8).[11] Concurrently, immunofluorescence demonstrated that the internalization of CCM caused a pronounced increase in PD-L1 expression on the target cell membrane, while CCM^{KO} and FM showed little impact (Figure 1N). Cellular uptake assay revealed intact FM internalization, evidenced by complete colocalization of membrane dyes, whereas simple mixtures remained segregated (Figure 1O). Finally, FM exhibited excellent drug-loading capacity. As illustrated in Figure S9, the maximum drug-loading capacities of Pt and Gem were 8.61% and 8.65%, respectively. Release profile indicated that FM presented better stability under neutral conditions and released more rapidly under acidic conditions, matching the

https://doi.org/10.1021/acsnano.5c14644
ACS Nano 2026, 20, 636−656

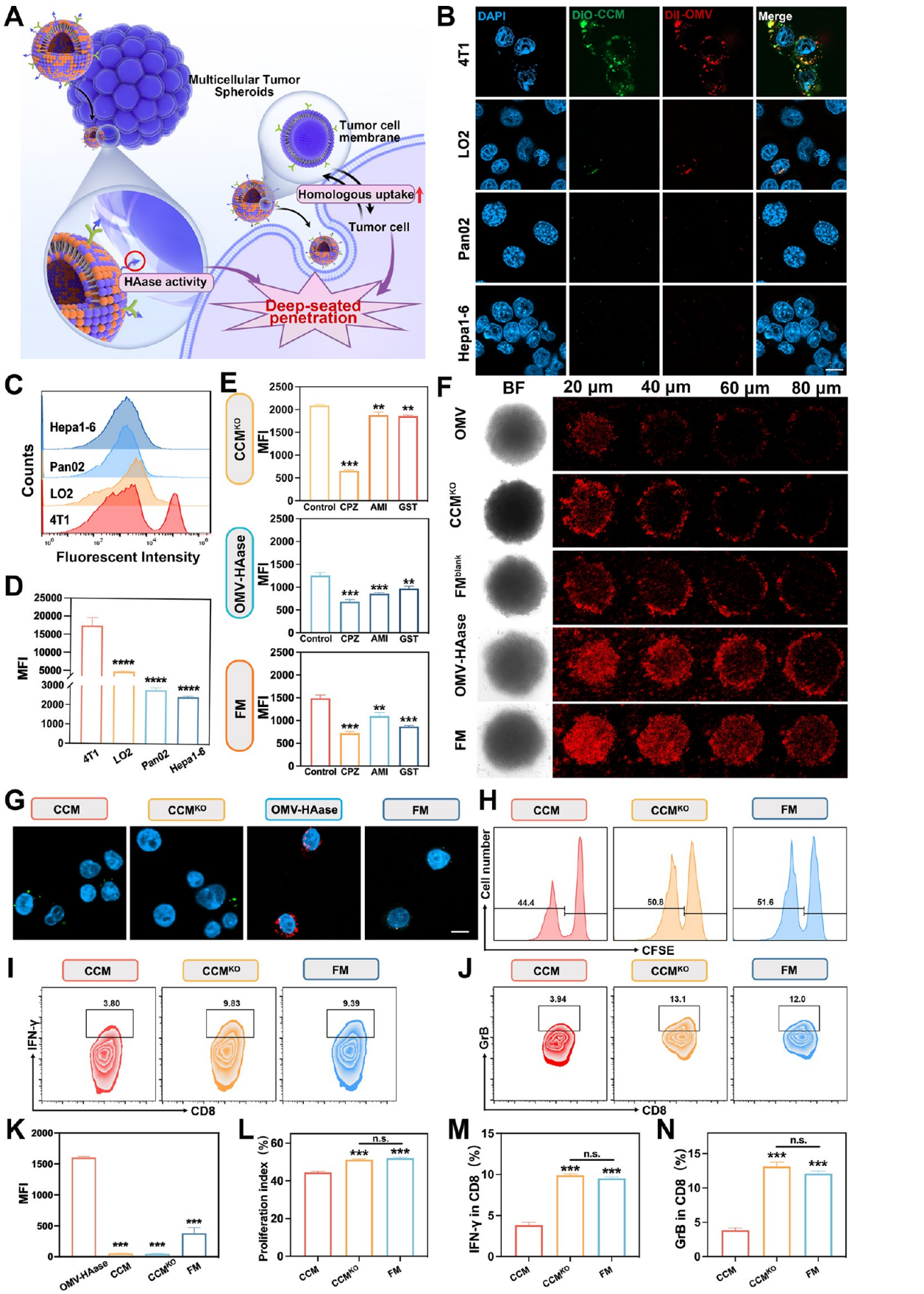

Figure 2. Homologous targeting, deep penetration, and immune-shielding of FM. (A) Schematic representation of the uptake and tumor penetration behavior of FM. (B) Confocal images depicting the uptake efficiency of FM by various cell models (scale bar: 10 μm). (C) Quantitative analysis of the uptake efficiency using flow cytometry and (D) statistics results. (E) Verification of the uptake mechanism of FM

https://doi.org/10.1021/acsnano.5c14644
ACS Nano 2026, 20, 636−656

Figure 2. continued

by flow cytometry. (F) Tumor spheroid penetration. (G) Phagocytosis of OMV-HAase, CCM^{KO}, and FM by Raw264.7 macrophages (scale bar: 10 μm). (H) CD8$^+$ T-cell proliferation level, (I) IFN-γ^+CD8$^+$ T-cell ratio, and (J) GrB$^+$ T-cell ratio in the coculture system. (K−N) Statistical analysis corresponding to Figure 2(G−J).

tumor environment. Postloading, particle size and morphology of FM remained unchanged, underscoring its superiority as an efficient delivery vehicle (Figure S10).

2.2. Homologous Targeting, Deep Penetration, and Immune-Shielding of FM. Benefiting from the reservation of an abundant array of specific adhesion proteins, antigens, and membrane structures, CCM inherit pertinent surface characteristics and functionalities.[32] Consequently, 4T1-derived FM exhibited highly selective binding and internalization by 4T1 cells, while minimal uptake was observed in other cell types (Figure 2A,B). Quantitative flow cytometry analyses revealed that 4T1-FM accumulation in 4T1 cells was 3.6-fold higher than that in normal hepatocytes and 7.1-fold higher than that in pancreatic cancer or hepatoma cells (Figure 2C,D). Similarly, Pan02-derived FM (Pan02-FM) demonstrated 2.8-, 9.0-, and 15.6-fold preferential uptake by Pan02 cells compared to other cell lines (Figure S11). Mechanistic study indicated that FM internalization was predominantly clathrin-mediated, with additional routes contributing cooperatively (Figure 2E). Importantly, FM efficiently delivered cargoes ranging from small molecules to macromolecular nucleic acids. Both payload cargoes demonstrated extensive intracellular colocalization with FM, while free siRNA remained largely extracellular (Figure S12). Although homologous targeting enhances tumor selectivity, the dense HA-rich still constitutes a formidable physical barrier to intratumoral diffusion.[33] By integration of HAase-decorated OMV, FM acquired potent ECM-degradation capacity, enabling deep tumor penetration (Figure 2A). In 3D tumor spheroids, blank OMV alone showed poor retention, CCM^{KO} accumulated only at surfaces, and HAase-free FM (FM^{blank}) penetrated modestly (Figure 2F). In stark contrast, OMV-HAase and FM demonstrated profound intraspheroidal distribution. Tumor cells evade innate immunity through "Don't eat me" signal.[34] Though the OMV was readily engulfed by macrophages, CCM, CCM^{KO}, and FM all exhibited pronounced resistance to phagocytosis (Figure 2G). Notably, PD-L1 removal did not compromise this immune-shielding property. CCM and CCM^{KO} were phagocytosed at comparable rates, indicating that CD47—abundantly retained on CCM^{KO}—remains the dominant inhibitory ligand for SIRP-α on macrophages. Quantitatively, the phagocytosis rate of FM decreased by 75.45% compared with that of the OMV (Figure 2K). Subsequently, we examined the immunomodulatory consequences of PD-L1 knockout. Tumor cells treated with CCM, CCM^{KO}, and FM were cocultured with CD8$^+$ T cell. Compared to CCM, both CCM^{KO} and FM significantly augmented CD8$^+$ T-cell proliferative (Figure 2H,L). Moreover, PD-L1-deficient vesicles elevated the ratio of IFN-γ^+CD8$^+$ T cells (Figure 2I,M) and enhanced Granzyme B (GrB) secretion (Figure 2J,N), underscoring that the elimination of PD-L1 from the vesicle membrane mitigates exogenous inadvertent immunosuppression. In summary, FM integrates three key advantages: (i) precise, homologous tumor targeting; (ii) ECM-disrupting, deep-penetration; (iii) robust immune-evasive properties. These features converge to deliver therapeutics efficiently and safely to the tumor core. Furthermore, by simply exchanging the CCM source, FM can be customized for tumor-specific applications, providing a versatile platform for precision cancer therapy.

2.3. Neutrophils Hitchhiking Delivery of FM. The optimal delivery behavior of a nanovehicle hinges on precise targeting of tumor regions and efficient recognition of target tumor cells. As previously mentioned, FM already demonstrates promising cellular-delivery precision and robust penetration through tumor stroma. Here, we dissect, in mechanistic detail, how FM exploits the ATR effect to accumulate within malignant tissue via NE hitchhiking (Figure 3A). NEs were harvested from the peripheral blood of C57BL/6 mice and purified to above 91.9%. Wright-Giemsa staining confirmed the characteristic lobular-shaped nuclei (Figure S13). Co-incubation assays revealed the efficient phagocytosis of both the OMV and FM by NEs, establishing the feasibility of FM hitchhiking (Figure 3B). Anti-TLR4 blockade markedly inhibited uptake, underscoring the TLR4-LPS axis as the dominant recognition pathway,[23] and confirming that FM retains the immunogenic surface signature of OMV. The uptake of FM was time- and dose-dependent, with FM stably entrapped inside NEs (Figure S14). Additionally, FM@Pt-loaded NE retained over 80% viability for 12 h, verifying the negligible premature leakage of the drug (Figure S15). To detect the chemotactic competence of FM, we established a transwell model recapitulating tumor necrosis factor (TNF-α)-driven tumor inflammation (Figure S16). Results demonstrated that the internalization of FM did not impair the chemotactic capability of NEs (Figures 3C and S17). Only under inflammatory conditions did NEs form neutrophil extracellular traps (NETs) and release FM,[35] with clear colocalization of NETs and FM (Figure S18). This suggested that FM-bearing NEs were stable under normal physiological conditions and released FM only upon reaching the tumor environment. With time, NETs were continuously produced with sustained FM release (Figure 3D). To rigorously assess FM structural integrity after NE-mediated uptake and subsequent release, FM membranes were labeled with DiI while FITC was encapsulated as a surrogate cargo. Flow cytometry analysis revealed that the FITC/DiI fluorescence ratio remained constant at 2 during both the uptake and NET-triggered release phases, confirming that FM vesicles retain their complete architecture and that no cargo leakage occurs throughout the NE-hitchhiking route (Figure S19).

In tumor-bearing mice, peripheral blood analysis at 4 h postintravenous injection revealed that compared to CCM (20.5%) and OMV (32.1%), FM exhibited stronger affinity to NEs, with a pronounced increase in the percentage of DiD$^+$-NEs (59.6%). TLR4 blockade collapsed FM-carrying NE percentage to 19.5%, underscoring the pivotal role of TLR4 in the hitchhiking process. By 24 h, the DiD$^+$-NEs ratio had risen further (Figure 3E,F). Furthermore, tumor tissues harvested 24 h postinjection contained 44% FM-bearing NEs, significantly higher than other groups (Figure S20). In vivo living imaging showed 1.36- and 1.12-fold higher FM accumulation in tumors relative to the OMV and CCM, respectively, at 48 h (Figure 3H). Notably, despite the inevitable nonspecific accumulation

https://doi.org/10.1021/acsnano.5c14644
ACS Nano 2026, 20, 636−656

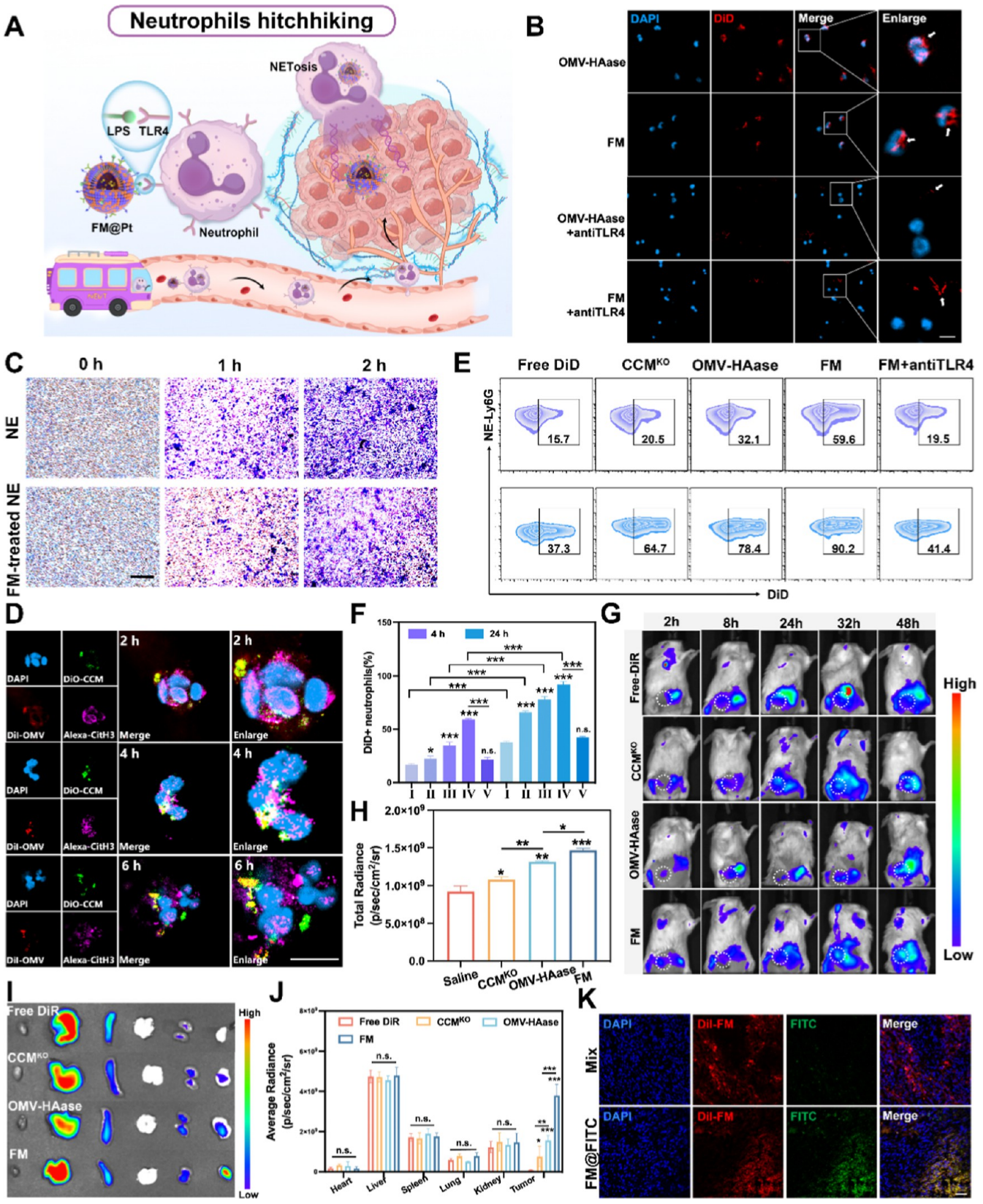

Figure 3. Neutrophils hitchhiking delivery of FM. (A) Schematic illustration of NE-mediated hitchhiking delivery of FM. (B) Phagocytosis of OMV and FM by NEs (DiD for nanovehicle staining, scale bar: 10 μm). (C) Chemotaxis of NEs before and after FM treatment under the tumor inflammatory environment. (D) NETs production of FM-carrying NEs (Alexa 647-CitH3 for NETs staining, scale bar: 10 μm). (E) Percentage of DiD^{+}-NEs at 4 and 24 h postintravenous injection (DiD for nanovehicle staining) and (F) its statistical analysis. (G) In vivo fluorescence imaging of postintravenous injection of free DiR, CCM, OMV and FM, and (H) statistical analysis of fluorescence intensity in tumor tissue at the 48th hour. (I) Fluorescence imaging of excised tissues from all groups and (J) its statistical analysis. (K)

https://doi.org/10.1021/acsnano.5c14644
ACS Nano 2026, 20, 636−656

Figure 3. continued

Immunofluorescence imaging of colocalization in tumor tissue (DiI for FM membrane labeling, FITC for cargo simulation, scale bar: 50 μm).

of nanoparticles in the liver and kidneys, FM exhibited the highest tumor-to-normal-organ ratio among all tested formulations (Figure 3G). Ex vivo imaging of excised tissues revealed markedly greater FM accumulation in the tumor—approximately 40-, 4.9-, and 2.4-fold higher than that observed in the other groups, respectively (Figure 3I,J). Finally, the immunofluorescence of tumor sections revealed a tight colocalization between DiI-labeled FM and FITC-represented cargo, confirming that NE-mediated delivery preserves FM integrity (Figure 3K). Collectively, FM inherits the OMV-derived TLR4-interactive membrane for efficient NE hitchhiking while leveraging CCM components to evade macrophage clearance. This dual-membrane engineering yields a nanoplatform with optimal tumor tropism, extended circulation, and intact therapeutic cargo delivery, setting the stage for next-generation cancer therapies.

2.4. In Vitro Immune Activation and Antitumor Efficacy. Initially, the cytotoxicity of individual components was profiled in the 4T1 cell (Figure 4A). CCM^{KO} alone showed negligible impact, whereas both OMV-HAase and FM elicited mild antiproliferative effects. By contrast, FM@Pt induced pronounced cytotoxicity. Analysis of typical apoptosis-related proteins revealed that FM did not affect cell apoptosis progress, while FM@Pt significantly accelerated tumor cell death (Figure 4B). We next examined the immunostimulatory potential of FM. Flow cytometry analysis exhibited exceptional ability to promote dendritic cell (DC) maturation, with a 1.75-fold increase compared with the control group (Figure 4C,D). Concurrently, FM interference led to the polarization of more M2 tumor-associated macrophages toward the M1 phenotype, as shown in Figure 4E−G. The representative images of macrophages treated with FM presented evident nuclear fragmentation and pseudopodia, indicative of M1 polarization (Figure S21). Therefore, FM demonstrated commendable immune activating properties, encompassing enhanced antigen presentation, immune response initiation, and direct tumoricidal effects. CCMs harbor numerous tumor antigens, which are derivatives of tumor whole cells, while OMVs yield PAMPs capable of interacting with pattern recognition receptors.[36] FM@Pt subsequently elicited strong immunogenic cell death (ICD), characterized by the exposure of calreticulin (CRT) on cell membranes, translocation of high-mobility group box 1 (HMGB1) from the nucleus, and extracellular release of adenosine triphosphate (ATP) (Figures 4H,I and S22). Compared with Pt, CCM^{KO}@Pt, and OMV-HAase@Pt, FM@Pt presented the strongest tumoricidal effects and showed the largest number of dead-cell in Calcein-AM/PI staining (Figure 4J,K). Apoptosis assays corroborated these findings, with total apoptotic fractions of 24.9%, 37.3%, 42.7%, and 50.8%, respectively (Figure 4L,M). In summary, FM serves as both an antigen-rich immune adjuvant and a stable chemotherapeutic vector. Its FM design maximizes immune activation while enabling precise drug delivery, thereby synergizing immunotherapy and chemotherapy for superior antitumor efficacy.

2.5. Antitumor Effect in Orthotopic Mouse Models of Triple Negative Breast Cancer. Encouraged by the promising delivery efficiency and robust antitumor activity observed in vitro, we subsequently evaluated the antitumor effect of FM@Pt on orthotopic mouse models of breast cancer. Hemolysis investigations preliminarily confirmed the excellent hemocompatibility of FM, with no hemolytic behavior at various concentrations (Figure S23). Afterward, 4T1 tumor-bearing mice were randomly assigned to five groups and, once tumors reached 200 mm^3, they were administrated saline, CCM^{KO}@Pt, OMV@Pt, OMV-HAase@Pt, and FM@Pt every 2 days for a total of five treatments (Figure 5A). Triple negative breast cancer (TNBC) is characterized by a dense HA-rich tumor matrix and a profound immunosuppression milieu (Figure 5B). Therefore, therapeutic success requires both ECM penetration and autoimmunity activation. After the treatment, the mice were euthanized, and tumor tissues were collected for weight and photograph. Body weight and tumor volume were monitored throughout the study period. Saline-treated mice exhibited rapid unchecked tumor growth. All the administration groups suppressed tumor progression, with FM@Pt achieving the most pronounced inhibition (Figure 5C,D). The average tumor volume alteration also reflected the maximum tumor suppression in the FM@Pt group (Figure 5E). Consistently, end-point tumor weights translated to inhibition rates in the four experimental groups were 38.84%, 56.22%, 68.53%, and 85.61%, respectively (Figures 5F and S24). Additionally, body weights remained stable across all groups, indicating minimal systemic toxicity (Figure 5G). To further investigate the potential therapeutic effect of FM@Pt, we evaluated cell proliferation and apoptosis levels using H&E, Ki67, and TUNEL staining, respectively (Figure 5H). H&E staining results revealed the most severe damage and necrosis of tumor cells in the FM@Pt group, while saline controls displayed closely packed, viable cells with prominent nuclei. Ki67 immunostaining demonstrated the lowest proliferation index in the FM@Pt group, while TUNEL assay showed maximal apoptotic signaling within the same group, confirming its potent antitumor activity. H&E sections of major organs revealed no pathological lesions, underscoring the favorable safety profile achieved by FM-mediated tumor-selective accumulation (Figure S25). In the survival experiment, FM@Pt significantly extended the survival time, whereas untreated mice succumbed rapidly to tumor burden (Figure 5I). In conclusion, FM@Pt exerts remarkable antitumor efficacy in the TNBC model by leveraging precise tumor targeting, robust ECM penetration, and efficient intratumoral drug accumulation while maintaining excellent systemic tolerability.

2.6. Immune Activation in Orthotopic Mouse Models of TNBC. Immunotherapy integrated with chemotherapy is emerging as a low-toxicity, high-efficacy paradigm for solid tumors. Yet most breast cancers are immunologically "cold", featuring scant immune infiltration and an immunosuppressive microenvironment.[37] Consequently, activating the innate immune system therefore offers a strategy to remodel the tumor microenvironment (TME) (Figure 6A). Based on our in vitro immune activation findings, we evaluated the impact of FM@Pt on autoimmune reactions in vivo, and typical gating strategies are shown in Figures S26−S29. Mature $CD80^+CD86^+$ DCs rose from 26.0% (saline group) to 50.5% (FM@Pt group) (Figure 6B,F). This robust DC maturation-

https://doi.org/10.1021/acsnano.5c14644
ACS Nano 2026, 20, 636−656

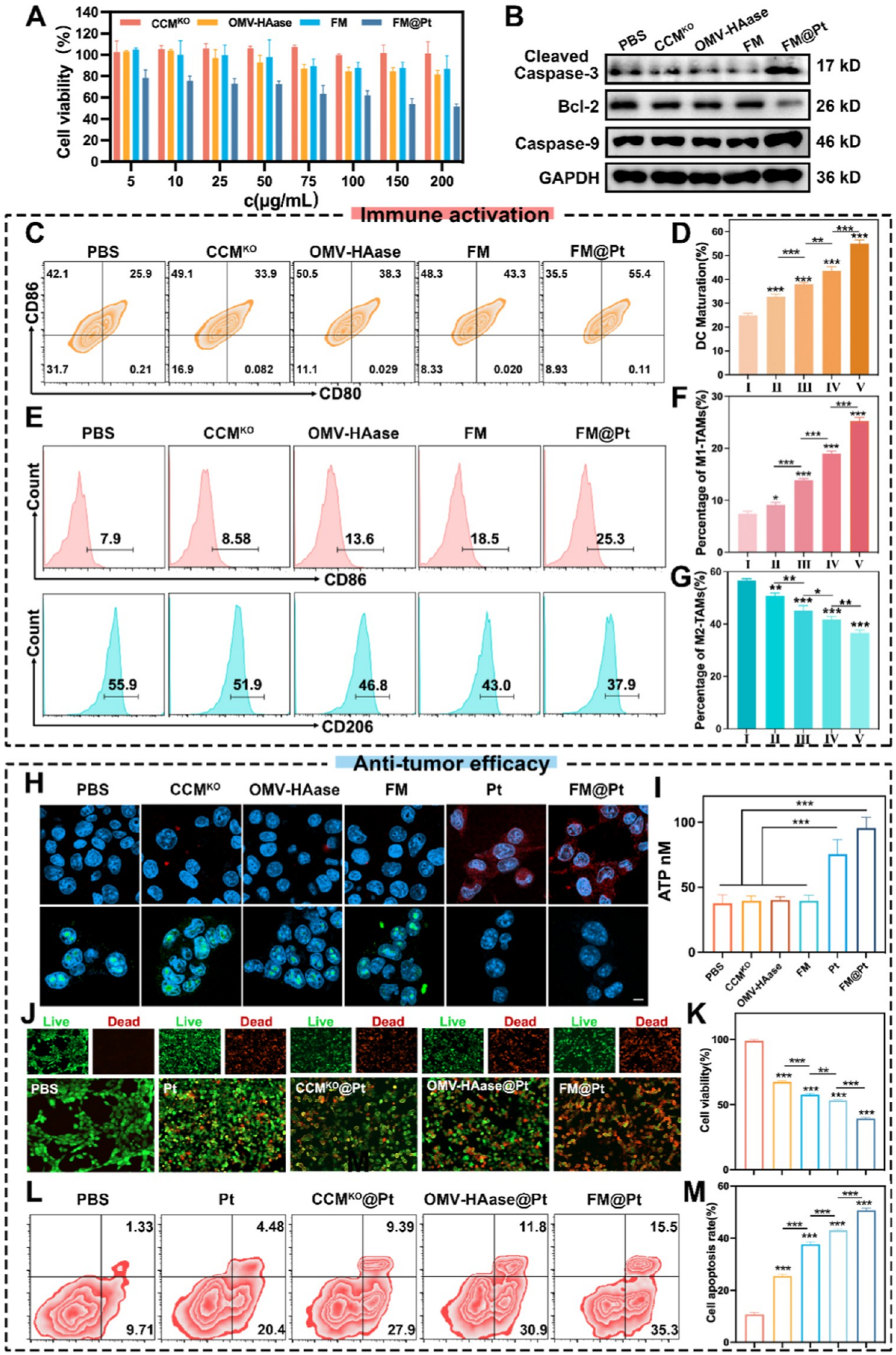

Figure 4. In vitro immune activation and antitumor efficacy of FM@Pt. (A) Cell viability at varying treatments and concentrations. (B) Western blot images of key apoptotic protein expression. (C) Flow cytometry analysis of DC maturation rates and (D) statistical results. (E) Flow cytometry analysis of the ratio of M1 and M2 macrophages and (F,G) statistical results. (H) Confocal analysis of CRT and HMGB1

https://doi.org/10.1021/acsnano.5c14644
ACS Nano 2026, 20, 636−656

Figure 4. continued

expression (scale bar: 10 μm). (I) Elisa analysis of the intracellular ATP content. (J) Representative live/dead stained images after different treatments and (K) statistical results. (L) Flow cytometry analysis of the cell apoptosis rate and (M) statistical results. (I: control group; II: CCM^{KO} group; III: OMV-HAase group; IV: FM group; V: FM@Pt group).

stimulating capacity stemmed from the synergy between the OMV-derived PAMPs and CCM-derived DAMPs. FM@Pt expanded the $CD8^+$ T-cell differentiation from 3.95% to 17.9%, significantly higher than other groups (Figure 6C,G). Moreover, the population of M2 macrophages in the FM@Pt group decreased significantly from 49.5% to 19.4%, accompanied by a notable increase of approximately 14% in M1 macrophages (Figure 6D,H). $CD4^+CD25^+Foxp3^+$ Tregs decreased from 12.4% to 4.33%, relieving local immunosuppression (Figure 6E,I). Immunofluorescence confirmed the most dense $CD8^+$ T-cell infiltration in FM@Pt-treated tumors (Figure 6J).

Subsequently, the tumors in saline and FM@Pt groups were, respectively, harvested and compared through transcriptome analysis (RNA-seq). A total of 342 genes were identified as significantly differentially expressed genes ($\log_2$ (FC) $\geq$ 0.58 (or ≤ -0.58), $p < 0.05$) (Figure S30). The specific expression levels of key genes related to immune system are exhibited in Figure S31. Gene Ontology analysis highlighted upregulated antigen presentation, lymphocyte activation, and adaptive immune responses (Figure S32). In the Kyoto Encyclopedia of Genes and Genomes (KEGG) analysis, the antigen processing and presentation of DCs, as well as the differentiation and activation of effector T cells, were strongly enriched (Figure 6K). Gene set enrichment analysis (GESA) further revealed significant enrichment of antigen processing and presentation (NES = 1.59, FDR = 0.05), T-cell receptor signaling pathway (NES = 1.69, FDR = 0.03), and natural killer cell-mediated cytotoxicity (NES = 1.80, FDR = 0.01) (Figure S33). Enrichment analysis of T-cell immune-related genes underlined enhanced selection, proliferation, differentiation, and activation (Figure 6L). Additionally, the intratumoral secretion levels of tumor necrosis factor-α (TNF-α), interleukin-6 (IL-6), and interferon-γ (IFN-γ) were obviously marked by FM@Pt (Figure 6M−O). The concentrations of these cytokines in the serum were also substantially increased, indicating the activation of antitumor systemic immunity (Figure S34). Summarily, FM, which is rich in tumor antigens and PAMPs, functions as a natural and effective immunoadjuvant. Engineered for superior tumor targeting and ECM penetration, FM@Pt precisely delivers Pt, induces ICD, and remodels the immunosuppressive TME, thereby orchestrating a synergistic chemo-immunotherapeutic attack against TNBC.

2.7. Antitumor and Immune Activation Effect in Orthotopic Mouse Models of Pancreatic Ductal Carcinoma. In addition to low immunogenicity and dense ECM, the limited permeability of pancreatic ductal carcinoma (PADC), stemming from inadequate vascularization, poses another significant therapeutic challenge (Figure 7A).[38,39] The conventional EPR-based accumulation of nanomedicines is therefore insufficient. Exploiting NE hitchhiking, FM emerges as a promising ATR strategy for drug delivery to PADC pathological tissues. We then investigated the applications of FM@Gem in orthotopic PADC models. In vivo living imaging showed FM@DiR exhibited a significant and progressive accumulation in tumor tissues (Figure S35). In isolated tumor tissues, the FM@DiR group showed the highest fluorescence intensity, while the OMV-HAase@DiR group also demonstrated considerable fluorescence enrichment (Figure 7B,C). Pancreatic tumors recruit NEs and trigger NETosis,[40,41] enabling OMVs to accumulate in PADC tissue via NE hitchhiking. The additional HAase-induced tumor stroma disruption and the CCM^{KO}-mediated evasion of macrophage clearance further amplified FM penetration, establishing an ATR route independent of EPR effects.

In PADC models, tumor fluorescence in the pancreatic tissue became clearly detectable by in vivo imaging on day 7 postinoculation, and treatment was initiated at this time according to the dosing schedule (Figure 7D). Throughout the administration period, no significant body weight loss was observed (Figure 7E). The bioluminescence imaging showed rapid tumor progression in the saline-treated group, whereas FM@Gem conferred the most potent tumor suppression (Figure 7F). The tumor inhibition rates of each treatment group were 38.8%, 56.7%, 72.4%, and 81.5%, respectively (Figure 7G). Moreover, FM@Gem markedly prolonged survival (Figure 7H). Histology further corroborated these findings (Figure 7I). Saline-treated tumors were densely packed and largely TUNEL-negative, whereas FM@Gem tumors displayed loose architecture and extensive apoptosis. Sirius red staining indicated ECM disruption in FM@Gem-treated tumors. In the Alcian blue staining, compared with the control group, the FM-treated group displayed less blue staining, confirming a reduction in the content of HA within the tumor stroma (Figure S36). HA degradation destroyed the ECM structure, facilitating deeper drug penetration and strengthening tumor damage. Despite the well-recognized immunosuppression, FM@Gem also potently remodeled TME. Compared to the control groups, FM@Gem induced substantial elevations in mature DC (10.4-fold), $CD8^+$ T-cell (3.8-fold), and M1 macrophage (2.8-fold), while concurrently suppressing Treg cell (0.24-fold) and M2 macrophage (0.16-fold) (Figures S37 and 7J−M). Collectively, FM overcomes the dual barriers of poor perfusion and immunosuppression in PADC. From TNBC to PADC, FM ensures precise tumor accumulation, deep stromal penetration, and robust immune conversion, highlighting its high versatility in treating various types of immune-cold tumors.

2.8. Persistent Antitumor Immunity in Distal Tumor Models. To determine whether FM@Pt elicits a durable and systemic immune response, we established a dual-tumor model (Figure 8A). The primary tumor size was consistently monitored throughout the whole experiment (Figure S38), and the growth of the distal tumor was also evaluated. The FM@Pt-treated group exhibited markedly smaller distal tumors (Figure 8B,C). Quantitative analysis toward tumor weight revealed distal tumor inhibition rates of 20.1% (Pt), 33.0% (FM), 54.5% (FM^{blank}@Pt), and 72.6% (FM@Pt) relative to the saline control group (Figure 8D). Moreover, FM@Pt pronouncedly prolonged the overall survival (Figure 8E). Body weight remained stable across all treatment groups (Figure 8F). Serum biochemistry, including alanine aminotransferase (ALT), aspartate aminotransferase (AST), total protein, albumin (ALB), creatinine (CREA) and urea, confirmed the absence of hepatic and renal toxicity (Figure

https://doi.org/10.1021/acsnano.5c14644
ACS Nano 2026, 20, 636−656

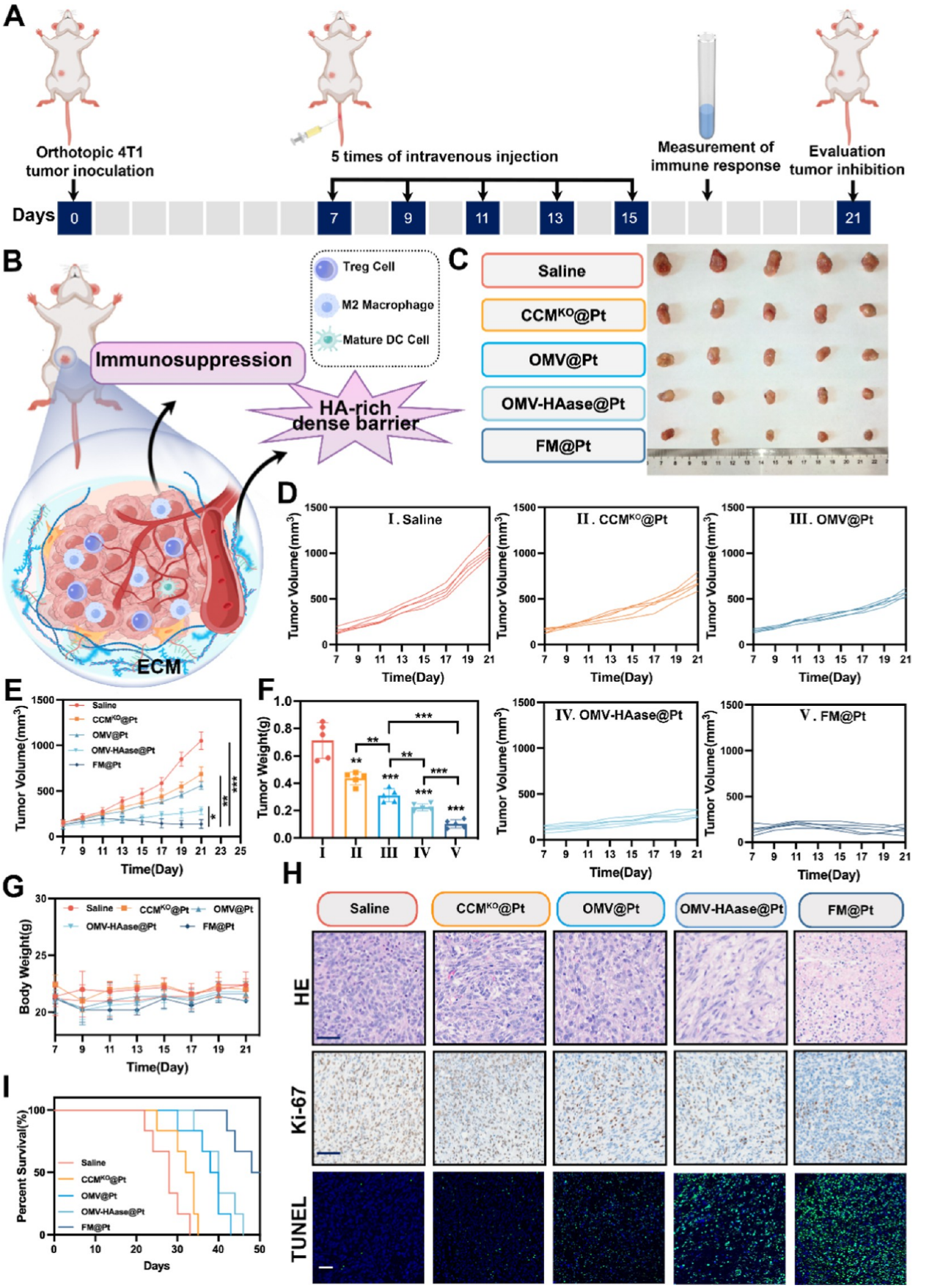

Figure 5. Antitumor effect in orthotopic mouse models of TNBC. (A) Illustration of the treatment schedule for primary tumor studies. (B) Schematic illustration of the typical characteristics in orthotopic breast cancer. (C) Photographs of tumor at the end point. (D) Curve of relative tumor volume changes and (E) mean tumor volume during treatment. (F) Tumor weight after the mice were euthanized. (G) Curve

https://doi.org/10.1021/acsnano.5c14644
ACS Nano 2026, 20, 636−656

Figure 5. continued

of body weight changes during treatment. (H) H&E, Ki67, TUNEL staining of tumor extracted from various groups. (I) Survival curve of mice calculated by the Kaplan−Meier estimate (scale bar: 50 μm).

8G). The key indicators of the blood routine examination further verified the excellent biosafety of FM@Pt (Figure S39), and the histological morphology of major organs following FM@Pt treatment revealed no signs of histological damage (Figure S40).

We next examined the immune basis of this distal protection. Splenic effector memory (Tem) ($CD62L^-CD44^+$) and central memory (Tcm) ($CD62L^+CD44^+$) T cells were quantified by flow cytometry. Compared with the control group, FM@Pt elevated $CD4^+$ Tem and Tcm percentages by 4.0- and 6.4-fold, respectively (Figure 8H,I), and increased $CD8^+$ Tem and Tcm by 3.6- and 5.6-fold, respectively (Figure 8J,K). GrB^+CD8^+ T cells rose from 7.66% (saline) to 28.6% (FM@Pt) (Figure 8L), and IFN-γ^+CD8^+ T cells rose from 5.33% to 31.4% (Figure 8M), underscoring the robust cytotoxic activity. The immunohistochemical results of CD8 corroborated these findings (Figure 8N). Systemic cytokine profiling further showed elevated TNF-α, IL-6, and IL-1β, consistent with potent immune activation (Figure 8O−Q). Notably, empty FM alone also induced modest immune responses and tumor suppression, highlighting its intrinsic immunomodulatory properties. Collectively, FM@Pt establishes a durable, systemic immunological memory that effectively prevents distal tumor outgrowth without overt toxicity.

2.9. Metastasis Suppression in 4T1 Lung Metastasis Models. Promoted by robust primary tumor control, we next assessed the antimetastatic ability of FM in an aggressive 4T1 lung metastasis model. Initially, the targeting efficacy of FM against pulmonary metastatic tumor tissues was studied. In vivo living imaging revealed prominent FM@DiR accumulation in pulmonary metastatic lesion within 8 h of intravenous injection, whereas free DiR was sequestered almost exclusively in liver (Figure 9A). FM^{blank} exhibited moderate tumor tropism with lower signal intensity, related to its general ECM penetration. Ex vivo organ imaging corroborated these findings. FM generated the brightest signal metastatic lung, while displaying relatively less off-target retention in the liver and kidneys (Figures S41 and 9B,C). Subsequently, the antimetastatic efficacy was evaluated in metastasis models (Figure 9D). Bioluminescence monitoring showed severe metastatic expansion in the saline-treated group, whereas FM@Pt significantly inhibited pulmonary outgrowth (Figure 9E). Compared with all other groups, lung from the FM@Pt-treated group demonstrated the lowest fluorescence burden and minimal bloating (Figure 9F,G). Quantitative analysis yielded metastasis inhibition rates of 14.0% (Pt), 22.9% (FM), 36.8% (FM^{blank}@Pt), and 60.7% (FM@Pt) relative to the saline group (Figure 9H). Empty FM alone exhibited intrinsic antimetastatic activity, highlighting its intrinsic immunomodulatory contribution. Additionally, membrane engineering via surface functionalization significantly augmented therapeutic efficacy compared to that of FM^{blank}@Pt. Lung metastasis significantly accelerated mortality in metastasis models, whereas FM@Pt markedly prolonged overall survival (Figure 9I). The histopathological examination of pulmonary tissues revealed a pronounced reduction in metastatic burden following FM@Pt treatment, as evidenced by decreased tumor nodule density in H&E sections (Figure 9J). Immunohistochemical analysis demonstrated an attenuated Ki67 proliferation index in metastatic lesions, further substantiating the therapeutic efficacy of FM@Pt (Figure 9K). Collectively, FM demonstrates superior tumor targeting, enhanced metastatic-site penetration, and potent therapeutic efficacy against tumor metastasis.

3. CONCLUSIONS

Effective antitumor therapies face substantial challenges from solid tumors' intricate microenvironments, particularly limited drug penetration/distribution within TME and inadequate immune activation. Traditional strategies relying solely on the EPR effect have shown limited clinical success, necessitating exploration of alternative mechanisms such as the ATR pathway. Here, we introduce a genetically engineerable biomimetic FM vehicle that integrates the distinctive properties of the OMVs and CCMs to address these challenges. OMV components exhibit high NE affinity, exploiting the inflammatory tropism of NEs to enable FM hitchhiking to tumor tissues. In this study, we observed the phagocytosis of the morphology of the OMVs in a normal environment and NETs formation under inflammatory stimuli, confirming the potential of NEs as active transport vectors. Consequently, FM achieves a large-scale, deep penetration into tumor tissues via NE-hitchhiking. Concurrently, CCMs endow FM with "don't eat me" CD47 signals, shielding it from mononuclear phagocyte clearance while enhancing tumor specificity. Upon reaching the tumor core, the dense HA-rich ECM poses the next hurdle. To overcome this, we incorporated HAase onto the OMVs, acting as a molecular drill to degrade the ECM and facilitate drug delivery and immune cell infiltration. We verified the HA degradation capacity and enhanced tumoral penetration, indicating that the introduction of HAase significantly improves FM delivery efficacy. Beyond delivery, FM functions as a potent immune adjuvant. The CCM layer presents a broad repertoire of tumor antigens, while the OMV layer supplies PAMPs for immune activation. Removal of PD-L1 from CCMs avoided the exogenous immune checkpoint introduction, reducing $CD8^+$ T-cell inhibition. In vitro studies confirmed the superior immune activation capacity of FM, promoting DC maturation and M2 macrophage polarization. Subsequently, the antitumor efficacy of drug-loaded FM systems was validated across multiple solid tumor models, including immunologically cold and refractory tumors, distal tumors, and lung metastatic lesions. Notably, FM@Pt exhibited robust antitumor activity while reversing immunosuppressive TMEs, achieving synergistic therapeutic outcomes through chemotherapeutic cytotoxicity and immune activation. In distal tumor and metastasis models, FM@Pt maintained a persistent antitumor immunity and significantly suppressed lesion growth. In PADC models, which are significantly lacking in vascularization and possess a highly dense ECM, FM still achieved superior tumor accumulation, confirming ATR as the primary pathway. Following FM@Gem treatment, tumor volume was markedly reduced, and survival was prolonged. Collectively, FM represents a multifunctional platform with

https://doi.org/10.1021/acsnano.5c14644
ACS Nano 2026, 20, 636−656

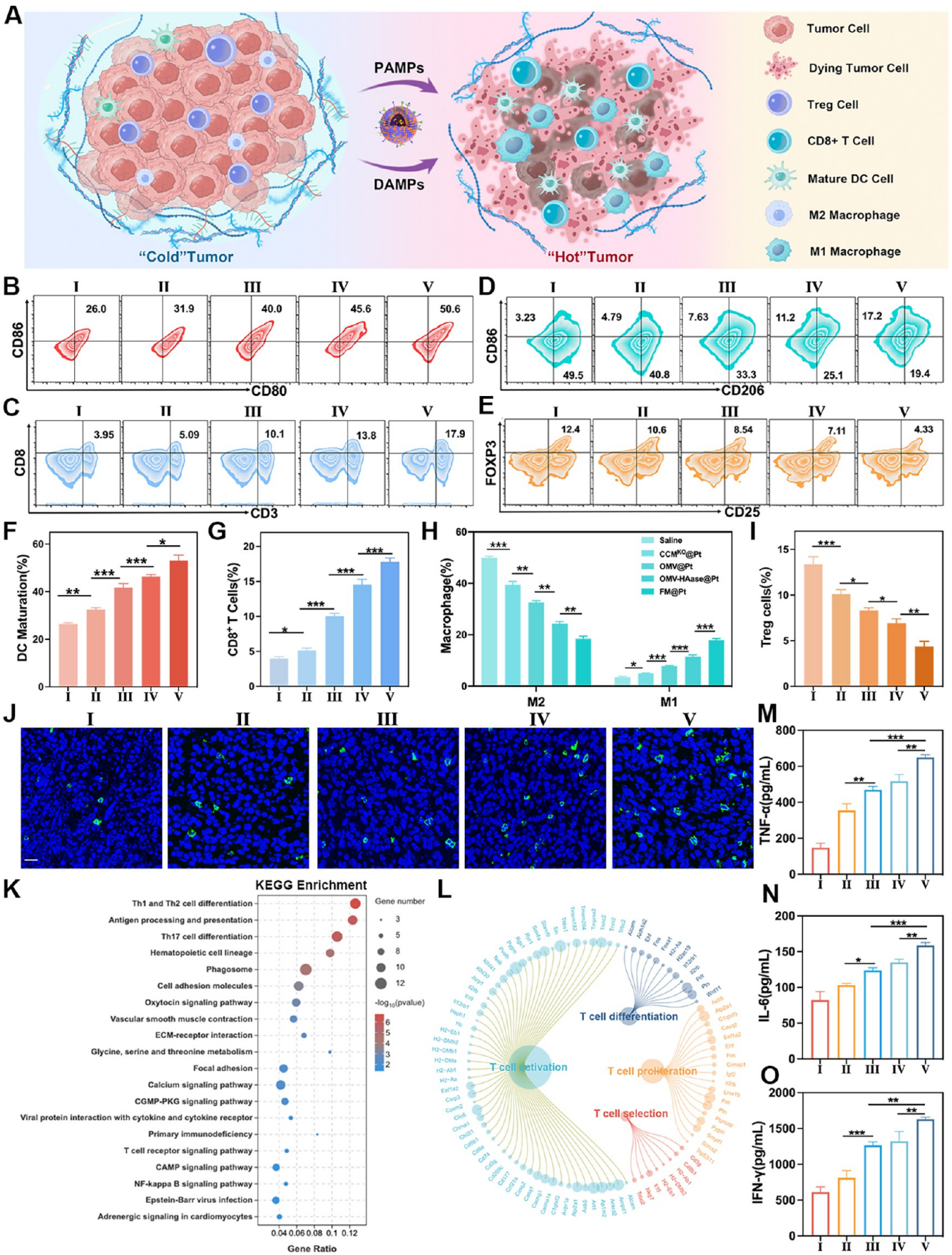

Figure 6. Immune activation in orthotopic mouse models of TNBC. (A) Schematic illustration of the transformation from immunosuppressive cold tumor to immune-activated hot state. Flow cytometry analysis of (B) mature DC proportion, (C) $CD8^+$ T-cell proportion, (D) macrophage phenotype, (E) Treg proportion, and (F–I) their corresponding statistical analysis. (J) Fluorescent images of

https://doi.org/10.1021/acsnano.5c14644
ACS Nano 2026, 20, 636–656

Figure 6. continued

CD8$^+$ T-cell infiltration in tumor tissue (scale bar: 50 μm). (K) KEGG pathway enrichment analysis of related specific pathway. (L) KEGG enrichment analysis of T-cell immune-related genes. The intratumoral secretion level of (M) TNF-α, (N) IL-6, and (O) IFN-γ measured by Elisa assay (I: saline group; II: CCM^{KO}@Pt group; III: OMV@Pt group; IV: OMV-HAase@Pt group, V: FM@Pt group).

three key advantages: precision delivery, ECM disruption, and potent immunomodulation. The modular customization capabilities and versatile compatibility of the FM platform establish a novel paradigm for advancing combination cancer therapy, enabling the plug-and-play integration of diverse therapeutic modalities. This adaptability positions FM as a transformative tool for personalized oncology, where treatment regimens can be rapidly tailored to individual tumor microenvironments and evolving resistance profiles.

4. METHOD

4.1. Materials. Plasmid pET30a-ClyA-Myc-HAase was synthesized by GenScript (Nanjing, China). *E. coli* BL21 (DE3) was purchased from Tolobio (Shanghai, China). β-D-thiogalactopyranoside (IPTG) was purchased from Sangon (Shanghai, China). Lysotracker Red and Annexin V-FITC/PI apoptosis kits were obtained from KeyGEN (Nanjing, China). DiO, DiI, bovine serum albumin (BSA), DAPI, crystal violet, bicinchoninic acid assay (BCA) kit, Coomassie brilliant blue, paraformaldehyde, Triton X-100, and cetyltrimethylammonium bromide (CTAB) were purchased from Beyotime (Shanghai, China). The protein marker standard and Western blot antibodies were purchased from Abclonal (Wuhan, China). Flow antibodies were purchased from Elabscience (Wuhan, China). All other chemicals were used as received without further purification.

4.2. Isolation of CCM^{KO} and OMV-HAase. The CRISPR-Cas9/sgRNA ribonucleoprotein complex (RNP) was assembled by mixing 1 μg of CRISPR-Cas9 protein with 0.5 μg of sgRNA and incubating at 37 °C for 10 min. Subsequently, 4T1 cells were seeded, and the RNP was transferred into cells by using the transfection reagent (Biodragon Biotechnology) for a duration of 6 h. The PD-L1 expression was assessed via Western blot. *E. coli* BL21cells were transformed with the plasmid pET30a-ClyA-Myc-HAase to generate engineered bacteria *E. coli*-HAase. To isolate CCM^{KO}, a cell membrane protein and cytoplasmic protein extraction kit (Beyotime, China) was employed. For OMV-HAase isolation, engineered *E. coli*-HAase was cultured under induction with 1 mM IPTG for 6 h. The culture supernatant was collected and filtered through a 0.45 μm vacuum filter. The filtrate was concentrated using Amicon centrifugal filters with a molecular-weight cutoff of 100 kDa (Millipore, USA), and OMV-HAase was subsequently isolated by ultracentrifugation at 200,000 g at 4 °C for 3 h. The protein concentration of CCM^{KO} and OMVs-HAase was determined using the BCA assay.

4.3. Preparation and Characterization of FM. The mixture of CCM^{KO} and OMV-HAase was prepared at a 1:1 ratio and subjected to ultrasonication in cold water for 10 min. Subsequently, the mixture was extruded 20 times to form FM. The protein components of FM were analyzed by 12% SDS-PAGE. The particle size and zeta potential of FM were measured using a Malvern Zetasizer (Nano ZS90, UK). The morphology of FM and its individual components was visualized by TEM (Hitachi Model H-7700 microscope, Japan).

4.4. In Vitro Internalization, Immune Escape, and Tumoral Penetration Behavior of FM. The cellular uptake efficiency of FM was evaluated in 4T1, Pan02, LO2, and Hepa1-6 cells using qualitative and quantitative methods. Confocal laser scanning microscopy (CLSM) (Carl Zeiss LSM700, Germany) and flow cytometry (FCM) (BD FACSCelesta, USA) were employed for the analyses. To visualize the components of FM, CCMKO and OMV-HAase were labeled with DiO and DiI, respectively. Cells were treated with DiO- and DiI-labeled FM for 4 h. Following incubation, the cells were stained with nuclear dye (DAPI, 10 μg/mL) for CLSM imaging. For FCM analysis, cells were incubated with FM, digested, and resuspended in PBS for detection. To elucidate the internalization mechanism of FM in 4T1 cells, three endocytosis inhibitors were used: chlorpromazine (CPZ, 8.5 μg/mL), genistein (GST, 50 μg/mL), and amiloride (AMI, 133 μg/mL). Cells were preincubated with each inhibitor for 1 h before being treated with FM for an additional 4 h. Cells were then collected for FCM analysis to assess the impact of these inhibitors on FM uptake. The immune escape capability of FM was investigated by using Raw264.7 macrophage cells. These cells were treated with DiI-labeled CCM^{KO}, OMV-HAase, and FM for 4 h, respectively. After treatment, Raw264.7 cells were fixed, stained with DAPI, and imaged using CLSM. Additionally, intracellular fluorescence intensity was quantified using FCM. The ability of FM to penetrate tumor spheroids was assessed using a 3D cell spheroid model. 4T1 cells were seeded into a 96-well 3D cell spheroid culture plate (Primesurface) at a density of 1×10^4 cells per well and cultured until uniform tumor spheres were formed. Tumor spheres were incubation with DiI-labeled CCM^{KO}, OMV, OMV-HAase, and FM for 4 h, and then tumor spheres were carefully taken out for CLSM detection.

4.5. In Vitro Internalization, Migration, and Release Behavior of FM by NEs. NEs were isolated from the femur and humerus of C57BL/6 mice using a Percoll gradient centrifugation method. Specifically, the resulting bone marrow eluates were collected, filtered through a 70 μm strainer, and resuspended in PBS. Red blood cells were lysed, and the cell suspension was layered onto a Percoll density gradient (55%, 65%, and 75%). The mixture was then centrifuged at 3000 rpm for 30 min at 25 °C. NEs were collected from the interface between the 65% and 75% Percoll layers. The purity of the isolated NEs was assessed by FCM, and their morphology was confirmed using Wright-Giemsa staining. To investigate the internalization mechanism of FM by NEs, the following treatments were applied: OMV-HAase, FM, OMV-HAase +anti-TLR4 (100 μg/mL), DiI-FM+anti-TLR4 (100 μg/mL). NEs were incubated with these treatments for 2 h, respectively. After incubation, cells were observed using CLSM. To investigate the migratory capacity, 4T1 cells were seeded into the lower chamber of a 24-well transwell plate (3 μm pore size, Corning Incorporated) for 12 h. Subsequently, NEs and NEs loaded with FM were added to the upper chamber, respectively. After incubation for 1, 2 h, cells that migrated to the lower membrane surface were fixed, stained with 0.1% crystal violet, and observed under an optical microscope. To

https://doi.org/10.1021/acsnano.5c14644
ACS Nano 2026, 20, 636−656

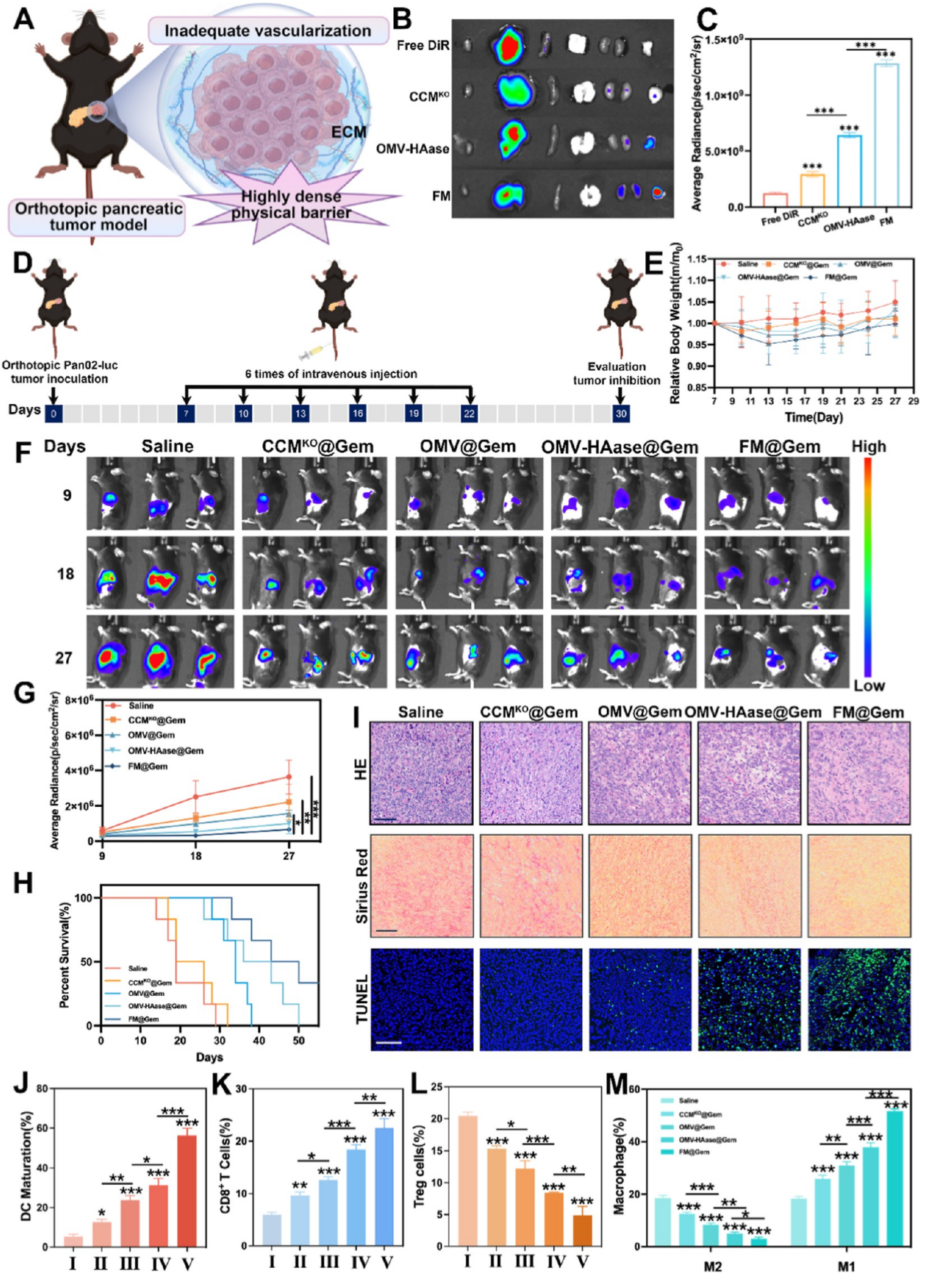

Figure 7. Antitumor and immune activation effect in orthotopic mouse models of PADC. (A) Schematic illustration of the typical characteristics in orthotopic PADC. (B) Fluorescence imaging of isolated tissues and (C) its statistical analysis. (D) Dosing cycle schematic. (E) Curve of body weight changes during treatment. (F) In vivo bioluminescence images and (G) relative statistical analysis of

https://doi.org/10.1021/acsnano.5c14644
ACS Nano 2026, 20, 636−656

Figure 7. continued

bioluminescence intensity. (H) Survival curve of mice calculated by the Kaplan−Meier estimate. (I) H&E, TUNEL, Sirius red staining of tumor extracted from various groups (scale bar: 50 μm). Quantitative analysis of (J) mature DC proportion, (K) CD8$^+$ T-cell proportion, (L) Treg-cell proportion, and (M) macrophage phenotype (cf. Figure S37).

study the release behavior of FM from NEs, NEs loaded with FM were treated with Phorbol 12-myristate 13-acetate (PMA, 100 ng/mL) for 2, 4, and 6 h. Cells were then fixed and permeabilized with 0.3% Triton X-100 for 25 min. After blocking with 5% BSA for 30 min, cells were incubated with the CitH3 antibody overnight, followed by a fluorescent secondary antibody for 60 min. Finally, the cells were imaged by using CLSM.

4.6. In Vivo Uptake of FM by NEs and Biodistribution of FM. To evaluate the uptake of OMV-HAase, CCM^{KO}, and FM by NEs, 4T1 tumor-bearing mice were intravenously injected with 3 mg/kg DiD-labeled OMV-HAase, CCM^{KO}, and FM, respectively. Additionally, part of the mice was administrated with TAK-242 to inhibit TLR4. Blood and tumor samples were collected 4 and 24 h postinjection. The collected cell suspensions were stained with PE-conjugated anti-Ly6G antibody to specifically identify NEs, and the uptake efficiency was analyzed by FCM. To monitor the biodistribution of CCM^{KO}, OMV-HAase, and FM, 4T1 tumor-bearing mice were injected with CCM^{KO}, OMV-HAase, and FM (3 mg/kg). In vivo fluorescence imaging was performed using a small animal in vivo imaging system (Tanon ABLX6, China) at 2, 5, 8, 24, 36, and 48 h postadministration. At 48 h, the mice were sacrificed, and major organs (heart, liver, spleen, lung, kidney) and tumors were isolated and imaged for fluorescence. To assess the stability and integrity of NE-delivered FM, mice were euthanized 24 h after tail vein injection of DiI-labeled-FM@FITC. Tumors were excised, embedded as frozen sections, and analyzed via confocal microscopy.

4.7. In Vitro Antitumor and Immune Activation Investigation. 4T1 cells were treated with PBS, CCM^{KO}, OMV-HAase, FM, and FM@Pt for 24 h, respectively. Then, the medium was replaced with 500 μL of Calcein AM/PI working solution, and cells were incubated at 37 °C for 30 min. Subsequently, cells were washed and observed using a cell imaging microplate detection system (Biotek, Cytation5, USA) to assess cell viability and cytotoxicity. Additionally, treated cells were harvested for further analysis of intracellular levels of apoptosis-related proteins, including Bcl2, caspase3, and caspase9. In apoptosis investigation, pretreated cells were resuspended in 500 μL of staining solution (with 5 μL of Annexin V-FITC and 5 μL of PI) for 20 min. The cell apoptosis rate was then detected by FCM. In immune study, pretreated cells were labeled with anti-CRT antibody and anti-HMGB1 antibody, followed by incubation with fluorescent secondary antibodies for CLSM detection. The intracellular ATP content was measured through the ATP Assay Kit (Beyotime, Shanghai, China). Subsequently, bone marrow-derived dendritic cells (BMDCs) were extracted from mouse tibial bone marrow. Pretreated cells were then coincubated with the BMDCs for 24 h using a Transwell system. BMDCs were harvested and stained with anti-CD80 and anti-CD86 for FCM analysis to assess immune activation. To investigate macrophage polarization, Raw264.7 cells were pretreated with 10 ng/mL IL-4 to induce M2 macrophages. Treated cells were seeded in the upper chamber of a Transwell plate, while M2 macrophages were placed in the lower chamber for 24 h coincubation. The morphology of the macrophages was observed under a microscope, the cells were collected for anti-CD80 and anti-CD206 staining, and the phenotype of macrophages was detected by FCM.

4.8. In Vivo Antitumor Therapeutic Effect on TNBC Mouse Models. All animal experiments were conducted in strict compliance with the requirements of the Institutional Animal Care and Use Committee of China Pharmaceutical University (Approval number: 2024-11-113). Female BALB/c mice (5−6 weeks, 18−22 g) received orthotopic implantation of 4T1 cells into the fourth mammary fat pad. The tumor (200 mm^3)-bearing mice were randomized into 5 groups receiving tail vein injections of: saline, CCM^{KO}@Pt, OMV@Pt, OMV-HAase@Pt, or FM@Pt on days 7−15 (once every 2 days). Tumor volume and body weight were monitored bi-daily until day 21, when tumors/major organs were harvested for ex vivo imaging and weighed. Additionally, tumor tissues were sectioned for H&E, immunofluorescence (TUNEL), and immunohistochemistry (K_i-67). Major organs were also harvested and sectioned for H&E staining to evaluate the biosafety. To further assess the long-term therapeutic impact and survival benefits, the experimental period was extended to 50 days. During this extended period, the survival rate of mice in each group was meticulously recorded.

4.9. In Vivo Immune Activation. The frequency of administration was consistent with that of the previously described protocol. On day 18, mice were sacrificed, and LN, spleen, and tumor tissues were extracted and processed through a series of steps: digestion (0.05 mg/mL collagenase), homogenate, filtration through 70 μm cell strainers, washing, and centrifugation (500g, 5 min). The resulting cell suspensions were incubated with specific antibody mixtures (DCs detection: anti-CD11c APC, anti-CD80 FITC, and anti-CD86 PE; macrophages: anti-CD45 V450, anti-F4/80 APC, anti-CD80 PE, anti-CD206 PE-CY7; CD8$^+$T cells: anti-CD45 V450, anti-CD3 FITC, anti-CD8 APC−CY7; Treg cells: anti-CD45 V450, anti-CD3 FITC, anti-CD4 PE, anti-CD25 APC, and anti-FOXP3 PerCP-CY5.5). Notably, FOXP3 is a nuclear protein, and CD206 is an intracellular protein. Hence, cells were subjected to a membrane permeabilization treatment before antibody labeling. After staining, cells were washed and suspended for FCM analysis. Additionally, tumor tissues were collected for CD8 IF staining. Serum and tumor tissue samples were collected for the detection of specific cytokines by ELISA kits, including TNF-α, IL-6, and IFN-γ.

4.10. In Vivo Antitumor Therapeutic Effect in PADC Mouse Models. Male C57BL/6 mice (6−8 weeks, 18−22 g) were orthotopically injected with Panc02 cells into the pancreatic tail. The tumor-bearing mice were randomized into five treatment groups and administered via tail vein injection with normal saline, CCM^{KO}@Gem, OMV@Gem, OMV-HAase@Gem, or FM@Gem on days 7, 10, 13, 16, 19, and 22 post-tumor inoculation. Mouse body weight was monitored every 3 days, while tumor volume was assessed every 9 days using the small animal imaging system. On day 30, mice were sacrificed, and tumors were harvested for imaging,

https://doi.org/10.1021/acsnano.5c14644
ACS Nano 2026, 20, 636−656

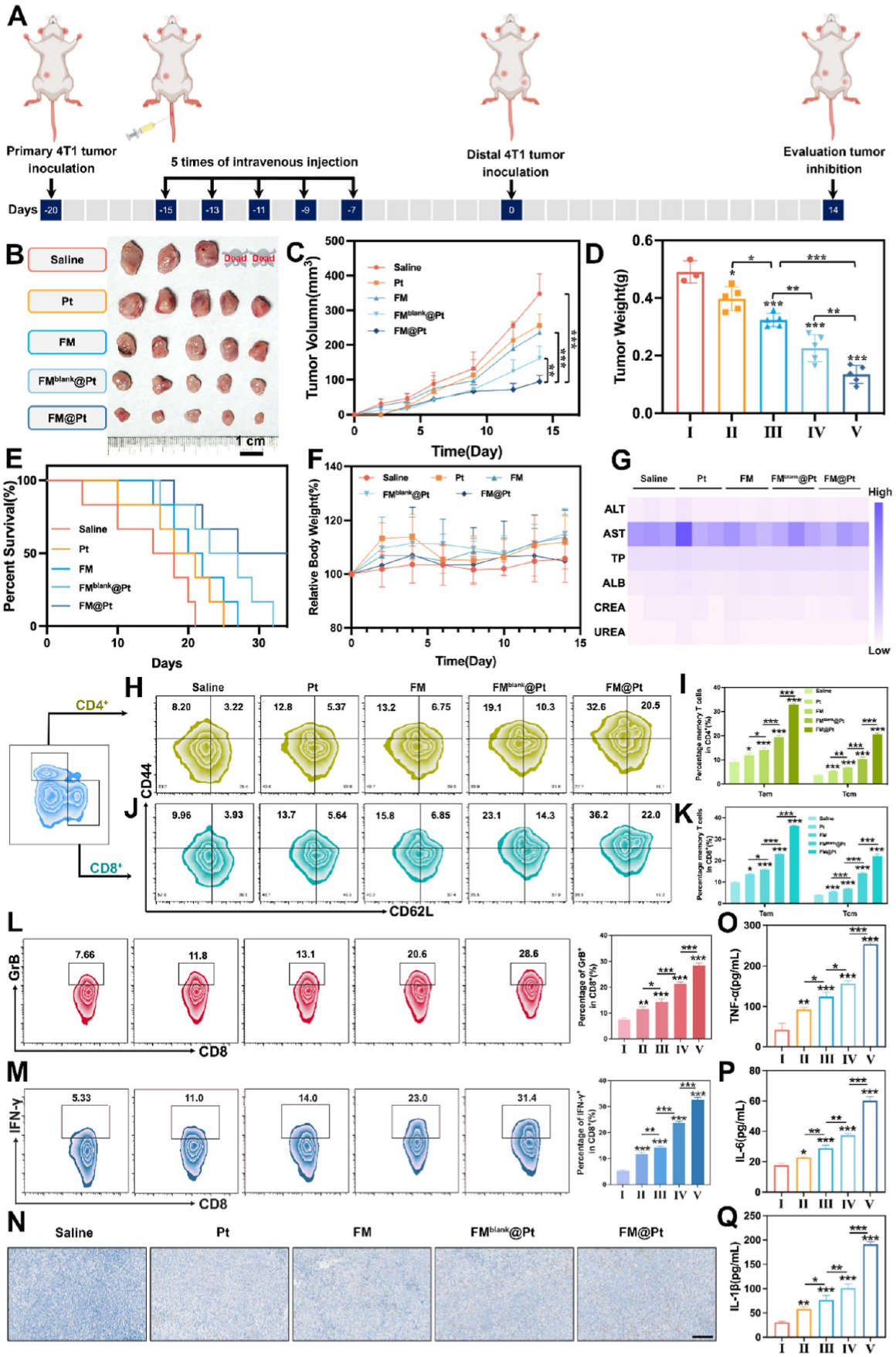

Figure 8. Persistent antitumor immunity in distal tumor models. (A) Schematic of distal tumor model construction. (B) Photographs of distal tumor at end point. (C) Curve of tumor volume. (D) Tumor weight after the mice were euthanized. (E) Survival curve. (F) Curve of body weight changes during treatment. (G) Serum biochemistry (ALT, AST, ALB, CREA, UREA). (H) Flow cytometric analysis of $CD4^+$

https://doi.org/10.1021/acsnano.5c14644
ACS Nano 2026, 20, 636−656

Figure 8. continued

Tcm and Tem percentages, and (I) its statistical results. (J) Flow cytometric analysis of $CD8^+$ Tcm and Tem percentages, and (K) its statistical results. (L) Flow cytometric analysis of GrB^+CD8^+ T-cell percentages and its statistical results. (M) Flow cytometric analysis of IFN-γ^+CD8^+ T-cell percentages and its statistical results. (N) CD8 immunohistochemical staining. The serum level of (O) TNF-α, (P) IL-6, and (Q) IFN-γ measured by ELISA (scale bar: 200 μm). (I: saline group; II: Pt group; III: FM group; IV: FM^{blank}@Pt group, V: FM@Pt group).

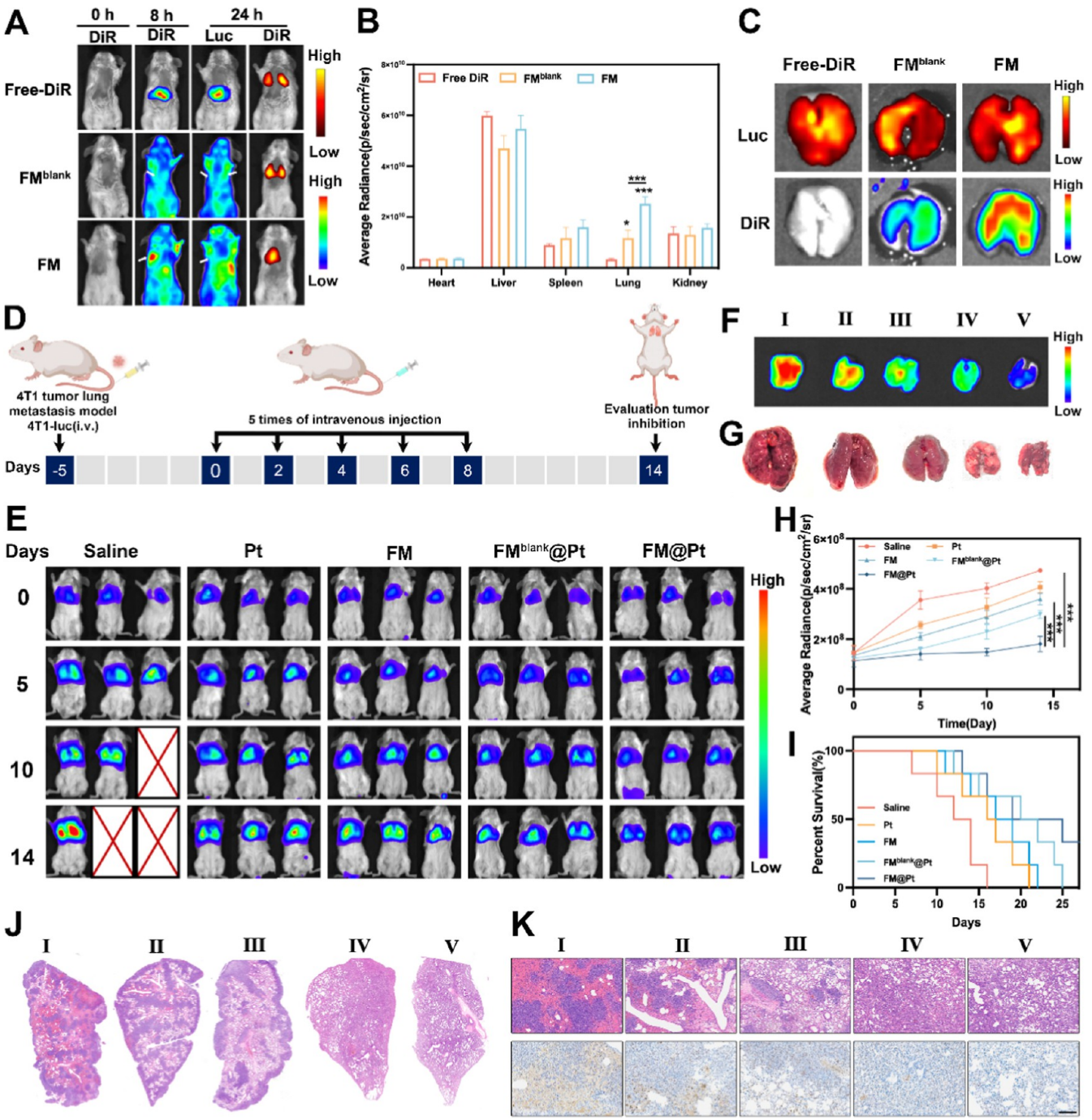

Figure 9. Metastasis suppression in 4T1 lung metastasis models. (A) In vivo fluorescence imaging of DiR distribution. (B) Statistical analysis of fluorescence intensity in major tissues. (C) Ex vivo fluorescence and bioluminescence overlays of metastatic lungs. (D) Schematic of lung metastasis suppression assay. (E) In vivo bioluminescence images. (F) Ex vivo bioluminescence images of excised lungs. (G) Lung photographs. (H) Statistical bioluminescence intensity analysis from in vivo imaging. (I) Survival curve. (J) H&E staining of lung tissues. (K) Higher-magnification H&E images and Ki67 staining (scale bar: 200 μm).

measurement, and weighing. Tumor tissues were sectioned for H&E, Sirius Red, and immunofluorescence (TUNEL) staining.

In the survival study, the experimental period was extended to 50 days, with survival recording for each group.

https://doi.org/10.1021/acsnano.5c14644
ACS Nano 2026, 20, 636−656

4.11. In Vivo Persistent Antitumor Immunity in Distal Tumor Models. Female BALB/c mice bearing 4T1 tumors (left breast, 40 mm^3) were randomized into five groups and intravenously administered normal saline, free Pt, FM, FM^{blank}@Pt, or FM@Pt on days −15, −13, −11, −9, and −7. On day 0, 4T1 cells (5×10^5/mouse) were subcutaneously inoculated into the right side. Tumor volume was tracked. Efficacy cohort analyses included tumor weight, volume, immunohistochemistry staining ($CD8^+$T cells), and serum biochemistry for safety assessment. For persistent immunity evaluation, the resulting cell suspensions were incubated with specific antibody mixtures (memory T cells: anti-CD45 V450, anti-CD3 R780, anti-CD8 APC-Cy7, anti-CD4 PE, anti-CD44 FITC, anti-CD62L APC; IFN-γ^+/GrB^+CD8^+T: anti-CD8 PE, anti-IFN-γ FITC, and anti-GrB PE-CY7). Serum samples were collected for the detection of specific cytokines by ELISA kits, including TNF-α, IL-6, and IL-1β.

4.12. In Vivo Metastasis Suppression in 4T1 Lung Metastasis Models. 4T1-luc cells were trypsinized, centrifuged, and resuspended in PBS to form single-cell suspensions (1×10^7 cells/mL). Following tail vein disinfection, 100 μL of the suspension was intravenously injected into BALB/c mice to establish a lung metastasis model. Successful model confirmation occurred 5 days postinjection. Mice were randomized into five groups and intravenously treated with saline, free Pt, FM, FM^{blank}@Pt, or FM@Pt on days 0, 2, 4, 6, and 8. Tumor burden was monitored every 5 days. On day 14, mice were sacrificed for lung imaging, H&E, and immunohistochemistry staining (Ki67). Long-term efficacy was evaluated through 30 day survival tracking.

4.13. Statistical Analysis. All results were presented as the mean ± SD statistical analysis from at least three independent experiments. A two-tailed *t*-test was performed, and $***p < 0.001$, $**p < 0.01$ and $*p < 0.05$ were considered statistically significant.

ASSOCIATED CONTENT

Supporting Information

The Supporting Information is available free of charge at https://pubs.acs.org/doi/10.1021/acsnano.5c14644.

Gene knockout verification; membrane fusion optimization; size distribution; enzyme activity assays of HAase; drug loading and release behavior; cellular uptake and delivery efficiency; verifications of NEs; internalization of FM by NEs; cell viability assay of NEs; NETosis assays; DiD^+-NEs percentage within tumors; macrophage polarization verification; hemolysis assay; H&E staining; gating logic of flow cytometry for immunology; RNA-seq; IFN-γ, TNF-α, and IL-6 levels in serum; biodistribution on PADC models; Alcian blue staining; immune activation investigation on PADC models; tumor volume; blood routine examination; ex vivo fluorescence imaging in metastasis models; and preparation of FM (PDF)

AUTHOR INFORMATION

Corresponding Authors

Zhenghong Wu − *Key Laboratory of Modern Chinese Medicines, China Pharmaceutical University, Nanjing 210009, China;* orcid.org/0000-0002-0244-329X; Phone: +86 15062208341; Email: zhenghongwu66@cpu.edu.cn

Xiaole Qi − *Key Laboratory of Modern Chinese Medicines, China Pharmaceutical University, Nanjing 210009, China; Industrial Technology Innovation Platform, Zhejiang Center for Safety Study of Drug Substances, Hangzhou 310018, China*; Phone: +86 25 83179703; Email: qixiaole523@cpu.edu.cn

Authors

Jia Zeng − *Key Laboratory of Modern Chinese Medicines, China Pharmaceutical University, Nanjing 210009, China*

Xinning Fang − *Key Laboratory of Modern Chinese Medicines, China Pharmaceutical University, Nanjing 210009, China*

Yuhan Li − *Key Laboratory of Modern Chinese Medicines, China Pharmaceutical University, Nanjing 210009, China*

Qi Yan − *Key Laboratory of Modern Chinese Medicines, China Pharmaceutical University, Nanjing 210009, China*

Yitong Li − *Key Laboratory of Modern Chinese Medicines, China Pharmaceutical University, Nanjing 210009, China*

Han Yu − *Key Laboratory of Modern Chinese Medicines, China Pharmaceutical University, Nanjing 210009, China*

Xiangyu Zhao − *Key Laboratory of Modern Chinese Medicines, China Pharmaceutical University, Nanjing 210009, China*

Mengyuan Xu − *Key Laboratory of Modern Chinese Medicines, China Pharmaceutical University, Nanjing 210009, China*

Complete contact information is available at: https://pubs.acs.org/10.1021/acsnano.5c14644

Author Contributions

[§]J.Z. and X.F. contributed equally to this work and should be considered co-first authors.

Notes

The authors declare no competing financial interest.

ACKNOWLEDGMENTS

This work was supported by the National Natural Science Foundation of China (No. 82373810) and the Jiangsu Pharmaceutical Association-Zhiyuan Pharmaceutical Peiying Jin Fund (No. J2024010).

REFERENCES

(1) Nguyen, D. T.; Baek, M. J.; Lee, S. M.; Kim, D.; Yoo, S. Y.; Lee, J. Y.; Kim, D. D. Photobleaching-mediated charge-convertible cyclodextrin nanoparticles achieve deep tumour penetration for rectal cancer theranostics. *Nat. Nanotechnol.* **2024**, *19* (11), 1723−1734.

(2) Dasgupta, A.; Sofias, A. M.; Kiessling, F.; Lammers, T. Nanoparticle Delivery to Tumours: From EPR and ATR Mechanisms to Clinical Impact. *Nat. Rev. Bioeng.* **2024**, *2* (9), 714−716.

(3) Kingston, B. R.; Lin, Z. P.; Ouyang, B.; MacMillan, P.; Ngai, J.; Syed, A. M.; Sindhwani, S.; Chan, W. C. W. Specific Endothelial Cells Govern Nanoparticle Entry into Solid Tumors. *ACS Nano* **2021**, *15* (9), 14080−14094.

(4) Naumenko, V. A.; Vlasova, K. Y.; Garanina, A. S.; Melnikov, P. A.; Potashnikova, D. M.; Vishnevskiy, D. A.; Vodopyanov, S. S.; Chekhonin, V. P.; Abakumov, M. A.; Majouga, A. G. Extravasating Neutrophils Open Vascular Barrier and Improve Liposomes Delivery to Tumors. *ACS Nano* **2019**, *13* (11), 12599−12612.

(5) Sindhwani, S.; Syed, A. M.; Ngai, J.; Kingston, B. R.; Maiorino, L.; Rothschild, J.; MacMillan, P.; Zhang, Y.; Rajesh, N. U.; Hoang, T.; Wu, J. L. Y.; Wilhelm, S.; Zilman, A.; Gadde, S.; Sulaiman, A.; Ouyang, B.; Lin, Z.; Wang, L.; Egeblad, M.; Chan, W. C. W. The entry of nanoparticles into solid tumours. *Nat. Mater.* **2020**, *19* (5), 566−575.

(6) Gao, C.; Wang, Q.; Li, J.; Kwong, C. H. T.; Wei, J.; Xie, B.; Lu, S.; Lee, S. M. Y.; Wang, R. In vivo hitchhiking of immune cells by intracellular self-assembly of bacteria-mimetic nanomedicine for targeted therapy of melanoma. *Sci. Adv.* **2022**, *8* (19), No. eabn1805.
(7) Li, W.; Little, N.; Park, J.; Foster, C. A.; Chen, J.; Lu, J. Tumor-Associated Fibroblast-Targeting Nanoparticles for Enhancing Solid Tumor Therapy: Progress and Challenges. *Mol. Pharmaceutics* **2021**, *18* (8), 2889−2905.
(8) Zhen, W. Y.; Weichselbaum, R. R.; Lin, W. B. Nanoparticle-Mediated Radiotherapy Remodels the Tumor Microenvironment to Enhance Antitumor Efficacy. *Adv. Mater.* **2023**, *35* (21), 2206370.
(9) Henke, E.; Nandigama, R.; Ergun, S. Extracellular Matrix in the Tumor Microenvironment and Its Impact on Cancer Therapy. *Front. Mol. Biosci.* **2020**, *6*, 160.
(10) Jalil, S. M. A.; Henry, J. C.; Cameron, A. J. M. Targets in the Tumour Matrisome to Promote Cancer Therapy Response. *Cancers* **2024**, *16* (10), 1847.
(11) Xu, S. Y.; Shi, X. X.; Ren, E.; Zhang, J. Z.; Gao, X.; Mu, D.; Liu, C.; Liu, G. Genetically Engineered Nanohyaluronidase Vesicles: A Smart Sonotheranostic Platform for Enhancing Cargo Penetration of Solid Tumors. *Adv. Funct. Mater.* **2022**, *32* (22), 2112989.
(12) Qiu, Z.-W.; Zhong, Y.-T.; Lu, Z.-M.; Yan, N.; Kong, R.-J.; Huang, J.-Q.; Li, Z.-F.; Nie, J.-M.; Li, R.; Cheng, H. Breaking Physical Barrier of Fibrotic Breast Cancer for Photodynamic Immunotherapy by Remodeling Tumor Extracellular Matrix and Reprogramming Cancer-Associated Fibroblasts. *ACS Nano* **2024**, *18* (13), 9713−9735.
(13) Rached, L.; Laparra, A.; Sakkal, M.; Danlos, F.-X.; Barlesi, F.; Carbonnel, F.; De Martin, E.; Ducreux, M.; Even, C.; Le Pavec, J.; Michot, J.-M.; Ribeiro, J. M.; Scotte, F.; Ponce Aix, S.; Lambotte, O.; Baldini, C.; Champiat, S. Toxicity of immunotherapy combinations with chemotherapy across tumor indications: Current knowledge and practical recommendations. *Cancer Treat. Rev.* **2024**, *127*, 102751.
(14) Galon, J.; Bruni, D. Approaches to treat immune hot, altered and cold tumours with combination immunotherapies. *Nat. Rev. Drug Discovery* **2019**, *18* (3), 197−218.
(15) Richter, M.; Vader, P.; Fuhrmann, G. Approaches to surface engineering of extracellular vesicles. *Adv. Drug Delivery Rev.* **2021**, *173*, 416−426.
(16) Mougenot, M. F.; Pereira, V. S.; Costa, A. L. R.; Lancellotti, M.; Porcionatto, M. A.; da Silveira, J. C.; de la Torre, L. G. Biomimetic Nanovesicles-Sources, Design, Production Methods, and Applications. *Pharmaceutics* **2022**, *14* (10), 2008.
(17) Raza, F.; Zafar, H.; Jiang, L.; Su, J.; Yuan, W.; Qiu, M.; Paiva-Santos, A. C. Progress of cell membrane-derived biomimetic nanovesicles for cancer phototherapy. *Biomater. Sci.* **2024**, *12* (1), 57−91.
(18) Le, Q. V.; Lee, J.; Lee, H.; Shim, G.; Oh, Y. K. Cell membrane-derived vesicles for delivery of therapeutic agents. *Acta Pharm. Sin. B* **2021**, *11* (8), 2096−2113.
(19) Meng, Z.; Zhang, Y.; Zhou, X.; Ji, J.; Liu, Z. Nanovaccines with cell-derived components for cancer immunotherapy. *Adv. Drug Delivery Rev.* **2022**, *182*, 114107.
(20) Zheng, C.; Zhong, Q.; Yi, K.; Kong, H.; Cao, F.; Zhuo, C.; Xu, Y.; Shi, R.; Ju, E.; Song, W.; Tao, Y.; Chen, X.; Li, M. Anti-phagocytosis-blocking repolarization-resistant membrane-fusogenic liposome (ARMFUL) for adoptive cell immunotherapy. *Sci. Adv.* **2023**, *9* (32), adh2413.
(21) Li, X.; Cheng, N.; Shi, D.; Li, Y.; Li, C.; Zhu, M.; Jin, Q.; Wu, Z.; Zhu, L.; He, Y.; Yao, H.; Ji, J. Sulfated liposome-based artificial cell membrane glycocalyx nanodecoys for coronavirus inactivation by membrane fusion. *Bioact. Mater.* **2024**, *33*, 1−13.
(22) Xie, B.; Zhao, H.; Ding, Y.-F.; Wang, Z.; Gao, C.; Li, S.; Zhang, K.; Ip, S. W.; Yu, H.; Wang, R. Supramolecularly Engineered Conjugate of Bacteria and Cell Membrane-Coated Magnetic Nanoparticles for Enhanced Ferroptosis and Immunotherapy of Tumors. *Adv. Sci.* **2023**, *10* (34), 2304407.
(23) Pan, J.; Wang, Z.; Huang, X.; Xue, J.; Zhang, S.; Guo, X.; Zhou, S. Bacteria-Derived Outer-Membrane Vesicles Hitchhike Neutrophils to Enhance Ischemic Stroke Therapy. *Adv. Mater.* **2023**, *35* (38), 2301779.
(24) Liu, G.; Ma, N.; Cheng, K.; Feng, Q.; Ma, X.; Yue, Y.; Li, Y.; Zhang, T.; Gao, X.; Liang, J.; Zhang, L.; Wang, X.; Ren, Z.; Fu, Y.-X.; Zhao, X.; Nie, G. Bacteria-derived nanovesicles enhance tumour vaccination by trained immunity. *Nat. Nanotechnol.* **2024**, *19* (3), 387−398.
(25) Chen, X.; Li, P.; Luo, B.; Song, C.; Wu, M.; Yao, Y.; Wang, D.; Li, X.; Hu, B.; He, S.; Zhao, Y.; Wang, C.; Yang, X.; Hu, J. Surface Mineralization of Engineered Bacterial Outer Membrane Vesicles to Enhance Tumor Photothermal/Immunotherapy. *ACS Nano* **2024**, *18* (2), 1357−1370.
(26) Feng, Q.; Ma, X.; Cheng, K.; Liu, G.; Li, Y.; Yue, Y.; Liang, J.; Zhang, L.; Zhang, T.; Wang, X.; Gao, X.; Nie, G.; Zhao, X. Engineered Bacterial Outer Membrane Vesicles as Controllable Two-Way Adaptors to Activate Macrophage Phagocytosis for Improved Tumor Immunotherapy. *Adv. Mater.* **2022**, *34* (40), 2206200.
(27) Peng, X.; Chen, J.; Gan, Y.; Yang, L.; Luo, Y.; Bu, C.; Huang, Y.; Chen, X.; Tan, J.; Yang, Y. Y.; Yuan, P.; Ding, X. Biofunctional lipid nanoparticles for precision treatment and prophylaxis of bacterial infections. *Sci. Adv.* **2024**, *10* (14), adk9754.
(28) Zou, M. Z.; Li, Z. H.; Bai, X. F.; Liu, C. J.; Zhang, X. Z. Hybrid Vesicles Based on Autologous Tumor Cell Membrane and Bacterial Outer Membrane To Enhance Innate Immune Response and Personalized Tumor Immunotherapy. *Nano Lett.* **2021**, *21* (20), 8609−8618.
(29) Chen, Z.; Li, Z.; Huang, H.; Shen, G.; Ren, Y.; Mao, X.; Wang, L.; Li, Z.; Wang, W.; Li, G.; Zhao, B.; Guo, W.; Hu, Y. Cancer Immunotherapy Based on Cell Membrane-Coated Nanocomposites Augmenting cGAS/STING Activation by Efferocytosis Blockade. *Small* **2023**, *19* (43), 2302758.
(30) Zhang, C.; Liu, Y.; Bai, T.; Shao, H.; Xiong, Z.; Epstein, M.; Li, X.; Chen, H. A novel member of biomimetic nano vesicles: Functional properties and research progress of hybrid-membered nanovesicles. *Biotechnol. Adv.* **2025**, *83*, 108637.
(31) Sun, M.; Shi, W.; Wu, Y.; He, Z.; Sun, J.; Cai, S.; Luo, Q. Immunogenic Nanovesicle-Tandem-Augmented Chemoimmunotherapy via Efficient Cancer-Homing Delivery and Optimized Ordinal-Interval Regime. *Adv. Sci.* **2023**, *10* (1), 2205247.
(32) Cui, J.; Zhang, F.; Yan, D. Y.; Han, T.; Wang, L.; Wang, D.; Tang, B. Z. "Trojan Horse" Phototheranostics: Fine-Engineering NIR-II AIEgen Camouflaged by Cancer Cell Membrane for Homologous-Targeting Multimodal Imaging-Guided Phototherapy. *Adv. Mater.* **2023**, *35* (33), 2302639.
(33) Zhao, Y.; Dong, Y.; Yang, S.; Tu, Y.; Wang, C.; Li, J.; Yuan, Y.; Lian, Z. Bioorthogonal Equipping CAR-T Cells with Hyaluronidase and Checkpoint Blocking Antibody for Enhanced Solid Tumor Immunotherapy. *ACS Cent. Sci.* **2022**, *8* (5), 603−614.
(34) Zhan, Z.; Zeng, W. Q.; Liu, J. Z.; Zhang, L.; Cao, Y.; Li, P.; Ran, H. T.; Wang, Z. G. Engineered Biomimetic Copper Sulfide Nanozyme Mediates "Don't Eat Me" Signaling for Photothermal and Chemodynamic Precision Therapies of Breast Cancer. *ACS Appl. Mater. Interfaces* **2023**, *15* (20), 24071−24083.
(35) Zeng, W.; Wang, Y.; Zhang, Q.; Hu, C.; Li, J.; Feng, J.; Hu, C.; Su, Y.; Lou, J.; Long, L.; Zhou, X. Neutrophil Nanodecoys Inhibit Tumor Metastasis by Blocking the Interaction between Tumor Cells and Neutrophils. *ACS Nano* **2024**, *18* (10), 7363−7378.
(36) Yang, M.; Zhou, J.; Lu, L.; Deng, D.; Huang, J.; Tang, Z.; Shi, X.; Lo, P.-C.; Lovell, J. F.; Zheng, Y.; Jin, H. Tumor cell membrane-based vaccines: A potential boost for cancer immunotherapy. *Exploration* **2024**, *4*, 20230171.
(37) Wu, B.; Zhang, B.; Li, B.; Wu, H.; Jiang, M. Cold and hot tumors: from molecular mechanisms to targeted therapy. *Signal Transduction Targeted Ther.* **2024**, *9* (1), 274.
(38) Luo, W.; Zhang, T. The new era of pancreatic cancer treatment: Application of nanotechnology breaking through bottlenecks. *Cancer Lett.* **2024**, *594I*, 216979.
(39) Tao, J.; Yang, G.; Zhou, W.; Qiu, J.; Chen, G.; Luo, W.; Zhao, F.; You, L.; Zheng, L.; Zhang, T.; Zhao, Y. Targeting hypoxic tumor

microenvironment in pancreatic cancer. *J. Hematol. Oncol.* **2021**, *14* (1), 14.
(40) Zhang, Y.; Chandra, V.; Riquelme Sanchez, E.; Dutta, P.; Quesada, P. R.; Rakoski, A.; Zoltan, M.; Arora, N.; Baydogan, S.; Horne, W.; Burks, J.; Xu, H.; Hussain, P.; Wang, H.; Gupta, S.; Maitra, A.; Bailey, J. M.; Moghaddam, S. J.; Banerjee, S.; Sahin, I.; et al. Interleukin-17-induced neutrophil extracellular traps mediate resistance to checkpoint blockade in pancreatic cancer. *J. Exp. Med.* **2020**, *217* (12), 20190354.
(41) Kajioka, H.; Kagawa, S.; Ito, A.; Yoshimoto, M.; Sakamoto, S.; Kikuchi, S.; Kuroda, S.; Yoshida, R.; Umeda, Y.; Noma, K.; Tazawa, H.; Fujiwara, T. Targeting neutrophil extracellular traps with thrombomodulin prevents pancreatic cancer metastasis. *Cancer Lett.* **2021**, *497*, 1−13.

https://doi.org/10.1021/acsnano.5c14644
ACS Nano 2026, 20, 636−656